Computers and Geotechnics 135 (2021) 104199

Contents lists available at ScienceDirect

Computers and Geotechnics

journal homepage: www.elsevier.com/locate/compgeo

Research Paper

A hybrid finite element model for non-isothermal two-phase flow in deformable porous media

S.A. Ghoreishian Amiri [a,*], E. Taheri [b], A.A. Lavasan [c]

[a] PoreLab, Department of Civil and Environmental Eng., Norwegian University of Science and Technology (NTNU), Trondheim, Norway
[b] Department of Rock Mechanics, Tarbiat Modares University, Tehran, Iran
[c] Chair of Soil Mechanics, Foundation Engineering and Environmental Geotechnics, Ruhr-Universität Bochum, Germany

ARTICLE INFO

Keywords:
Multiphase flow
Geomechanic
Thermal flow
THM coupling
Hybrid solution

ABSTRACT

This paper presents a numerical method to model the coupled thermo-hydro-mechanical (THM) processes in porous media saturated with two immiscible fluids. The basic equations of the system have been derived based on the averaging theory, considering skeleton deformation, two-phase fluid flow, and heat transport. As applying the standard Galerkin finite element method (GFEM) to solve this system of partial differential equations may lead to oscillatory results for saturation and temperature profiles, a hybrid numerical solution is proposed. In this frame, the GFEM is combined with a control volume based finite element (CVFE) approach, and a streamline upwind control volume finite element (SUCVFE) scheme, respectively for the mechanical, hydraulic and thermal part of the system. The CVFEM has been adopted to provide a smooth saturation profile by ensuring local mass conservation, while the streamline upwind scheme has been applied to remove the spurious temperature oscillation by adding stabilizing terms to the thermal part of the system. The CVFE and SUCVFE formulations have been derived using a similar approach as the standard FE practice in the context of weighted residual technique, but using different weighting functions. This will significantly facilitate the implementation of the proposed model in existing FE codes. Accuracy and efficiency of the proposed method have been justified using several numerical examples and comparing the results with available analytical or numerical solutions.

1. Introduction

Numerical simulation of coupled THM phenomena in geological porous media is of great interest in many engineering disciplines. Areas of applications include, among the others, natural gas and oil recovery, geothermal energy utilization, underground waste repositories, geological sequestration of CO_2, underground gas storage, artificial ground freezing and cold climate engineering. Generally, the basic governing equations of the above-mentioned systems, i.e. the momentum, mass and energy conservation laws, are derived using either the continuum theory of mixture (Nunziato and Walsh, 1980; Passman, 1977; Wei and Muraleetharan, 2002), local volume averaging theory (Hassanizadeh and Gray, 1979a, 1979b; Lewis and Schrefler, 1998), or a phenomenological extension of Biot's consolidation theory (McTigue, 1986; Pao et al., 2001; Schiffman, 1971). Although, these approaches are generally suitable for describing coupled THM phenomena in porous media, the formers may introduce a more systematic and flexible framework for further development.

Many attempts, with different coupling strategies, have been made to develop numerical tools for analyzing this kind of problems. Sequential coupling using different codes for thermal, multiphase fluid flow and geomechanics is one of the most popular strategies (Asadi and Ataie-Ashtiani, 2021; Kim, 2018; Lee et al., 2019; Rutqvist, 2011; Rutqvist et al., 2002). It has a wide flexibility in terms of software development and can be computationally less costly comparing to a fully coupled scheme. However, stability, accuracy and convergence properties of the solution might be affected (Kim, 2018). On the other hand, a fully coupled solution offers an unconditional stability and internal consistency as the full system of equations are solved together. A number of studies have been conducted to develop fully coupled THM models in a single integrated code, utilizing different numerical schemes associated with their intended applications (Abed and Sołowski, 2017; Cui et al., 2018; Kelkar et al., 2014; Nishimura et al., 2009; Pao et al., 2001; Tong et al., 2010; Winterfeld and Wu, 2016; Zhou and Ghassemi, 2009). The most extensively used discretization scheme has been the FEM (Abed and Sołowski, 2017; Cui et al., 2018; Lewis and Schrefler, 1998;

* Corresponding author.
E-mail address: seyed.amiri@ntnu.no (S.A. Ghoreishian Amiri).

https://doi.org/10.1016/j.compgeo.2021.104199
Received 30 September 2020; Received in revised form 22 March 2021; Accepted 21 April 2021
Available online 5 May 2021

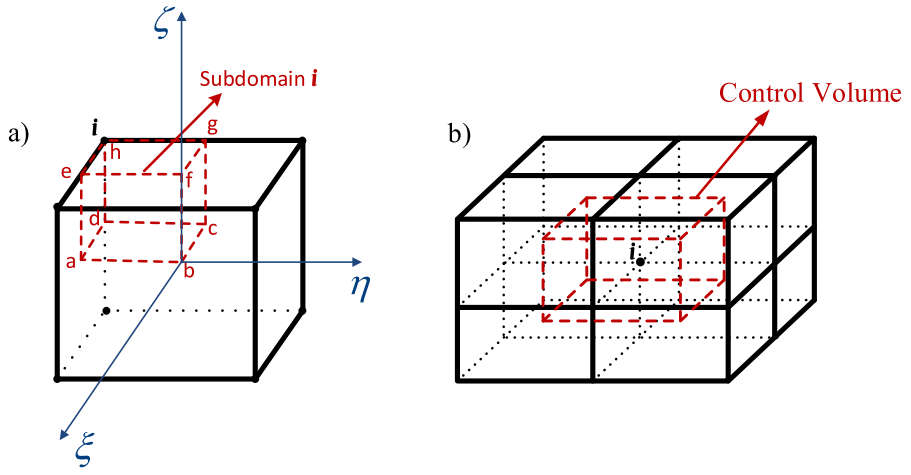

Fig. 1. Schematic representation of subdomain (a); and control volume (b) around node i.

Nishimura et al., 2009; Pao et al., 2001; Tong et al., 2010; Zhou and Ghassemi, 2009). Several fully coupled solution procedures using FEM are presented and investigated in Lewis and Schrefler (1998). Despite the advantages of the FEM in dealing with complex geometries and unstructured grids, it does not, in its standard form (i.e. standard Galerkin solution), automatically satisfy the local conservation of the transported variables between adjacent elements. As shown by Hughes et al. (2000), GFEM could be locally conservative if the flux is calculated in a correct way through a post-processing step. However, it will add another layer of complexity to the system (Wan, 2002). Nevertheless, a non-conservative solution might result in severe nonphysical oscillation of the field variables, especially in case of reservoir simulation with a distinct saturation shock front. Indeed, the GFEM results in a spurious temperature oscillation in case of convection-dominated thermal flow. In order to overcome these issues, hybrid solutions are desirable.

Despite the popularity of the GFEM as the natural choice to discretize the momentum balance equation, it is not the optimum choice for transport equations. On the other hand, the finite volume method (FVM) is one of the most popular methods in transport problems, as it is known to satisfy the local conservation of the transported variables. Kelkar et al. (2014) proposed a fully coupled THM model using a combination of the GFE and FV methods for geomechanics and transport equations (mass and heat), respectively. The proposed solution is fully conservative in terms of mass and heat, and capable of representing complex geometries using an unstructured FV scheme. However, the vertex-centered FV scheme, employed in this work for the transport equations, is not fully compatible with the FE discretization of the deformation equations. The FV part of the model needs the nodal values of volumetric strains, while in the FE part, strains are computed at integration points, which does not necessarily provide a continuous nodal value to be used by the FV part. This issue might affect stability and accuracy of the solution.

The FVM is flexible to be enriched by the basis functions of the FEM to interpolate the variation of the field variables over the control

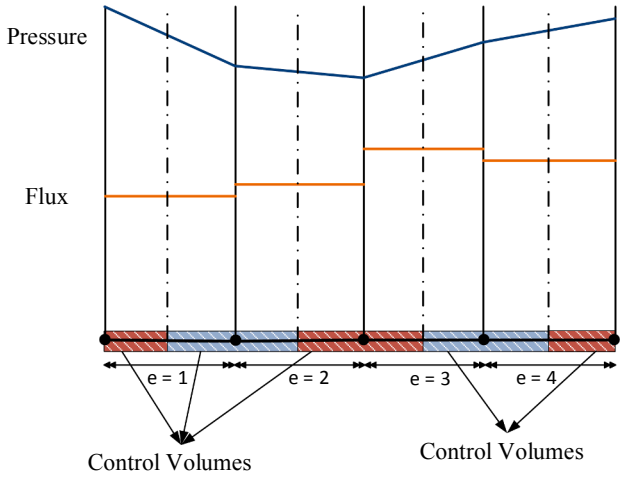

Fig. 2. Pressure and flux distribution in a one-dimensional case: flux discontinuity between the adjacent elements (Sadrnejad et al., 2012).

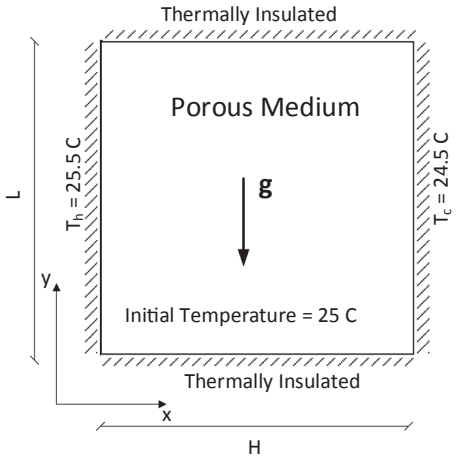

Fig. 3. The natural convection problem: domain and boundary conditions (dimension: 0.1 × 0.1 m).

Table 1
Material properties for the natural convection problem.

Water density at reference condition, ton/m^3	$\rho_{w_{ref}} = 1$
Reference temperature, °C	$T_{ref} = 15.5$
Rock density, ton/m^3	$\rho_s = 2.4$
Water viscosity, kPa.s	$\mu_w = 1.5 \times 10^{-6}$
Rock porosity, %	$n = 40$
Absolute permeability, m^2	$K = 1 \times 10^{-8}$
Specific heat capacity of water, kJ/ton.K	$C_w = 4181$
Specific heat capacity of rock, kJ/ton.K	$C_s = 835$
Thermal conductivity of the mixture, kJ/s.m.K	$\chi = 0.7027 \times 10^{-3}$

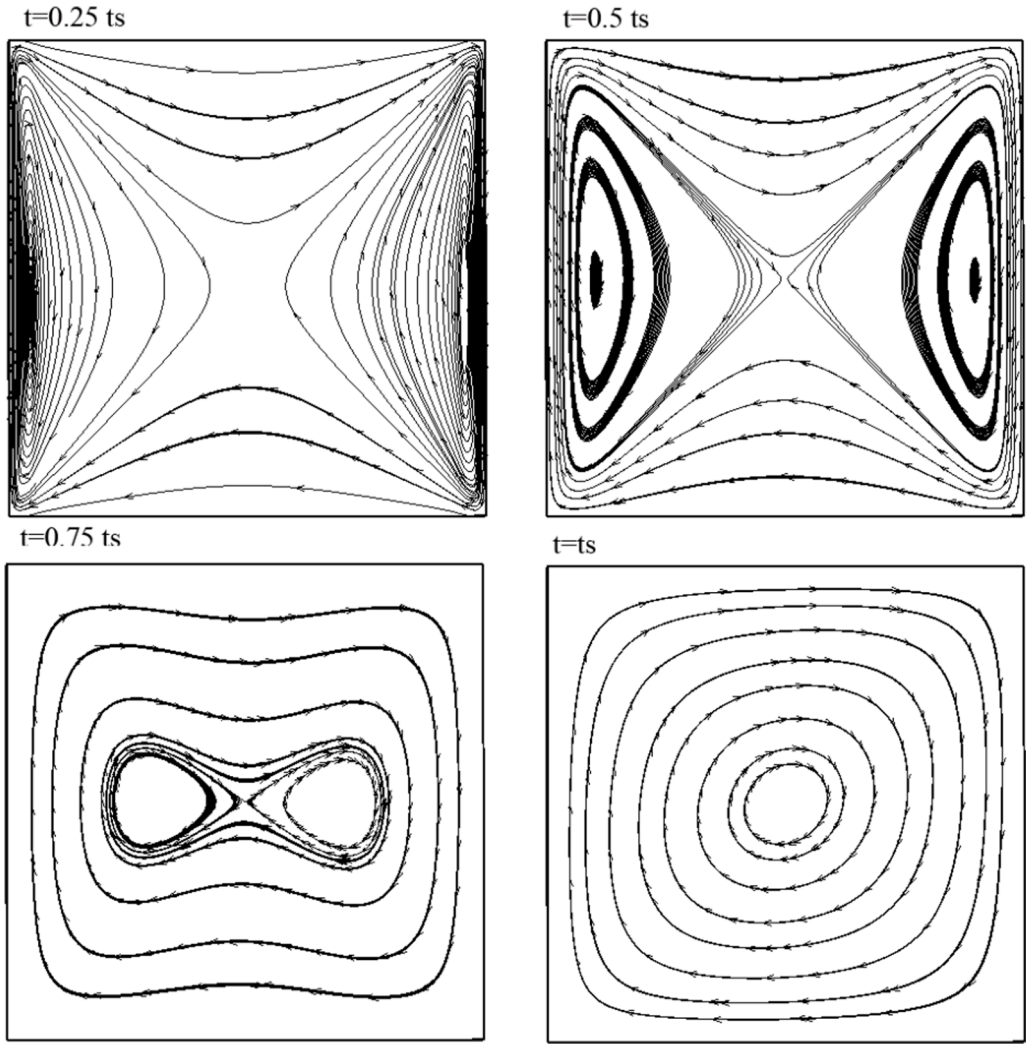

Fig. 4. Streamlines at different time before the steady state, ts, for the natural convection problem-Case 1.

volumes and their boundaries. This will make the FV and FE schemes more compatible. This approach is known as the CVFEM in the computational fluid dynamic literature (Chen et al., 2005; Forsyth, 1990; Fung et al., 1992; Ghoreishian Amiri et al., 2013; Gottardi and Dall'Olio, 1992; Mello et al., 2009; Sadrnejad et al., 2012; Verma, 1996). Flexibility of the CVFEM, along with its conservative characteristic and compatibility with the FEM, makes the method an attractive option for a hybrid numerical solution of coupled THM systems. A hybrid solution of this type has been proposed by Ghoreishian Amiri et al. (2017) for coupled hydro-mechanical problems, and its efficiency was demonstrated through several benchmark problems.

In this study, a fully coupled model, with a combination of the CVFEM (for mass), SUCVFEM (for heat) and GFEM (for deformation), is presented. We shall see that the CVFE formulation could be obtained in the context of the FE technology by employing different type of weighting functions. This is beneficial for implementing purposes, especially in existing FE codes, since it makes possible to construct the final set of the algebraic equations using the traditional assembling algorithm of the FEM. Indeed, the need for the so-called dual mesh system, which is normally necessary in hybrid models, will also be obviated. In this context, the control volumes are automatically constructed around each node using appropriate weighting functions, and provides a fully conservative solution.

2. Governing equations

The system of concern is a non-isothermal deformable porous medium saturated with two immiscible fluids (wetting and non-wetting phases). In this study, no phase change is considered; and local thermal equilibrium is assumed. The multiphase system is described using the assumption of superposition; i.e. any spatial point, $\boldsymbol{x}$, in the solution domain, is simultaneously occupied by material points of all phases, $\boldsymbol{X}_\alpha$, while their motions are described independently.

A Lagrangian description is used for the solid skeleton, while the fluid phases are described in Eulerian form with respect to the motion of the solid skeleton. Relative velocities are, therefore, defined as:

$$\bar{\boldsymbol{v}}_\alpha = \boldsymbol{v}_\alpha - \boldsymbol{v}_s, \ \alpha \neq s \tag{1}$$

where $\boldsymbol{v}_\alpha$ and $\boldsymbol{v}_s$ are the absolute velocities of phase α and solid skeleton, respectively, and $\bar{\boldsymbol{v}}_\alpha$ denotes the relative velocity.

In this description, the material time derivative of any differentiable function given in the spatial coordinate, $f_\alpha(\boldsymbol{x},t)$, should then be referred to the solid skeleton:

$$\frac{D^s f_\alpha}{Dt} = \frac{\partial f_\alpha}{\partial t} + (\nabla f_\alpha).\boldsymbol{v}_s \tag{2}$$

where $\frac{D^s f_\alpha}{Dt}$ indicates the material time derivative of function f (in phase α) with respect to the solid skeleton, and ∇ is the gradient operator.

By assuming a quasi-static condition with irrotational velocity field,

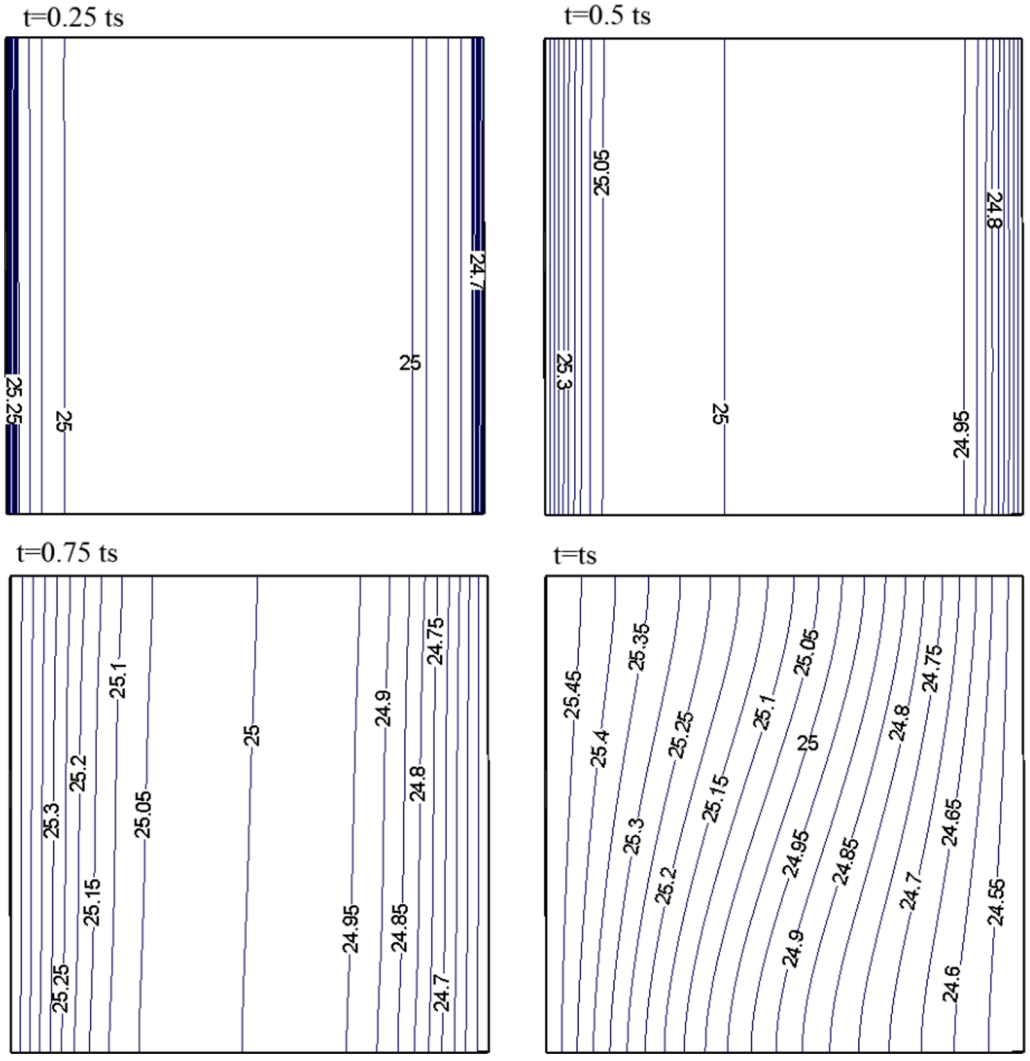

Fig. 5. Temperature isotherms at different time before the steady state, ts, for the natural convection problem-Case 1.

small displacements and displacement gradients, the following relations are hold:

$$\frac{\partial f}{\partial \boldsymbol{x}} \approx \frac{\partial f}{\partial \boldsymbol{X}} \tag{3}$$

$$\nabla^T \boldsymbol{v}_s = -\boldsymbol{m}^T \frac{D^s \boldsymbol{\varepsilon}}{Dt} \tag{4}$$

$$\boldsymbol{\varepsilon} = -\mathcal{L}\boldsymbol{u} \tag{5}$$

where $\boldsymbol{u}$ denotes the displacement vector of the solid skeleton, ∇^T is the divergence operator, and $\boldsymbol{\varepsilon}$, $\mathcal{L}$ and $\boldsymbol{m}^T$ are defined as:

$$\boldsymbol{\varepsilon} = [\varepsilon_{xx} \quad \varepsilon_{yy} \quad \varepsilon_{zz} \quad \gamma_{xy} \quad \gamma_{yz} \quad \gamma_{zx}]^T \tag{6}$$

$$\mathcal{L} = \begin{bmatrix} \frac{\partial}{\partial x} & 0 & 0 & \frac{\partial}{\partial y} & 0 & \frac{\partial}{\partial z} \\ 0 & \frac{\partial}{\partial y} & 0 & \frac{\partial}{\partial x} & \frac{\partial}{\partial z} & 0 \\ 0 & 0 & \frac{\partial}{\partial z} & 0 & \frac{\partial}{\partial y} & \frac{\partial}{\partial x} \end{bmatrix}^T \tag{7}$$

$$\boldsymbol{m} = [1 \quad 1 \quad 1 \quad 0 \quad 0 \quad 0]^T \tag{8}$$

where the superscript T refers to transpose. It should be noted that throughout this article, compressive stress and strain are assumed to be positive.

2.1. Mass balance equations

The mass balance equation for the solid phase might be written as:

$$\frac{D^s[(1-n)\rho_s]}{Dt} + (1-n)\rho_s \nabla^T \boldsymbol{v}_s = 0 \tag{9}$$

where ρ_s is the density of solid grains and n is the porosity. Assuming incompressible solid grains, and a volumetric thermal expansion coefficient, β_s, one can write:

$$d\rho_s = -\rho_s \beta_s dT \tag{10}$$

where T is temperature. By substituting Eqs. (4) and (10) into (9), the

Table 2
Comparison of the average Nusselt number for the natural convection problem.

	Nithiarasu et al. (1997)	Massarotti (2001)	Lauriat and Prasad (1989)	Present model
Average Nusselt number	1.08	1.07	1.07	1.08

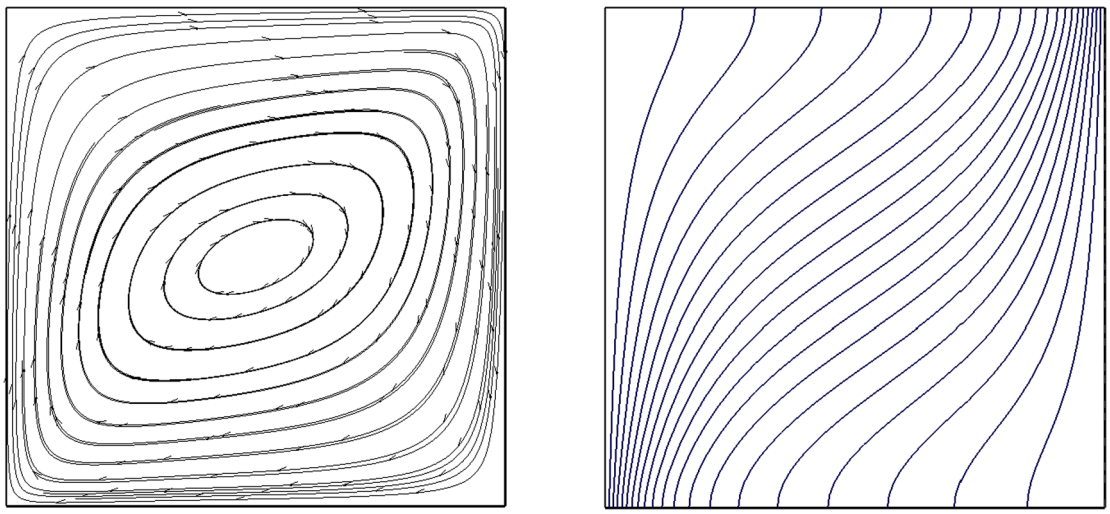

Fig. 6. Steady state streamlines and temperature isotherms for the natural convection problem-Case 2.

Table 3
Material properties for the hot water injection problem.

Water density at reference condition, kg/m^3	$\rho_{w_{ref}} = 1000$
Reference temperature, °C	$T_{ref} = 15.5$
Reference pressure, kPa	$p_{ref} = 101$
Rock density, kg/m^3	$\rho_s = 2386$
Rock porosity, %	$n = 18.67$
Total pore compressibility, vol/vol.kPa	$K_p = 1.45 \times 10^{-6}$
Water compressibility, vol/vol.kPa	$K_w = 4.35 \times 10^{-7}$
Absolute permeability, darcy	$K = 0.089$
Specific heat capacity of water, kJ/kg.K	$C_w = 4.18$
Specific heat capacity of rock, kJ/kg.K	$C_s = 0.837$
Thermal conductivity of the mixture, W/m.K	$\chi = 2.5$
Thermal expansion of water, vol/vol.K	$\beta_w = 8.82 \times 10^{-4}$
Thermal expansion of rock, vol/vol.K	$\beta_s = 2.7 \times 10^{-5}$

following expression can be found for variation of porosity:

$$dn = -(1-n)\boldsymbol{m}^T d\boldsymbol{\varepsilon} - (1-n)\beta_s dT \tag{11}$$

Similarly, the mass balance equations of the fluid phases are written as:

$$\frac{D^s[n_\alpha \rho_\alpha]}{Dt} + \nabla^T(n_\alpha \rho_\alpha \bar{\boldsymbol{v}}_\alpha) + n_\alpha \rho_\alpha \nabla^T \boldsymbol{v}_s - \dot{M}_\alpha = 0, \ \alpha \neq s \tag{12}$$

where n_α denotes the volume fraction of phase α and $\dot{M}$ is the source/sink term. The relative velocities of the fluids are described using the generalized Darcy's law:

$$n_\alpha \bar{\boldsymbol{v}}_\alpha = \frac{k_{r\alpha}\boldsymbol{K}}{\mu_\alpha}[\rho_\alpha \boldsymbol{g} - \nabla p_\alpha], \ \alpha \neq s \tag{13}$$

where $\boldsymbol{g}$ is the gravitational acceleration vector, p stands for pressure, $\boldsymbol{K}$ is the absolute permeability tensor, μ denotes dynamic viscosity and k_r is the relative permeability that is related to the volume fraction of the wetting phase, n_w:

$$k_{rw} = \mathscr{A}(\mathrm{n_w}) \tag{14}$$

$$k_{rn} = \mathscr{G}(\mathrm{n_w}) \tag{15}$$

where the subscripts w and n refer to the wetting and non-wetting fluids, respectively.

Fluids interaction can be considered using empirical correlations relating the capillary pressure, $p_c = p_n - p_w$, and temperature to the volume fraction of the wetting phase (Hassanizadeh and Gray, 1993):

$$n_w = \mathscr{T}(\mathrm{p_c}, \mathrm{T}) \tag{16}$$

Indeed, the following constraint must be satisfied:

$$n_w + n_n = n \tag{17}$$

By partially differentiating of Eqs. (16) and (17), and introducing Eq.

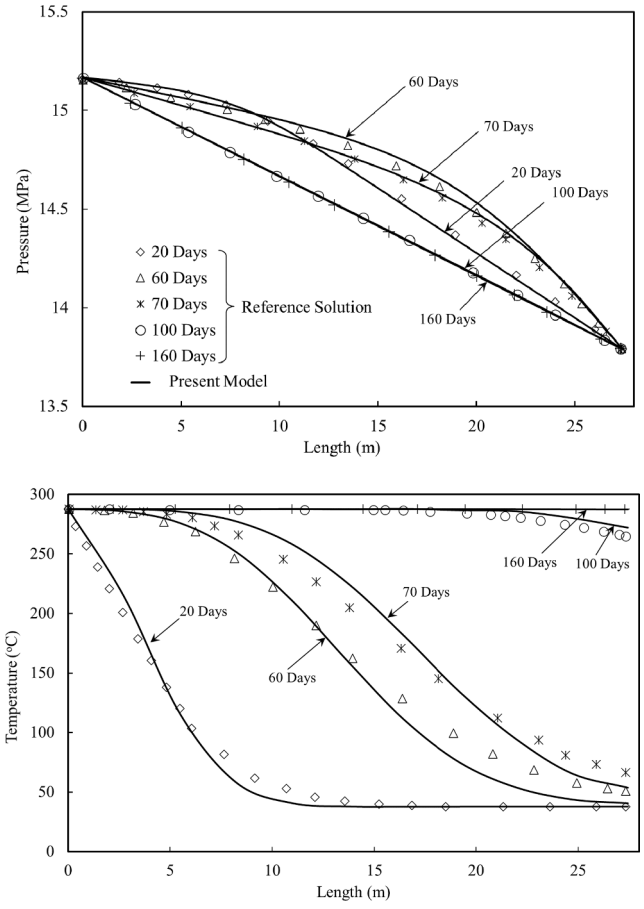

Fig. 7. Pore pressure and temperature profiles at different times at the center line of the reservoir, compared to Pao et al. (2001).

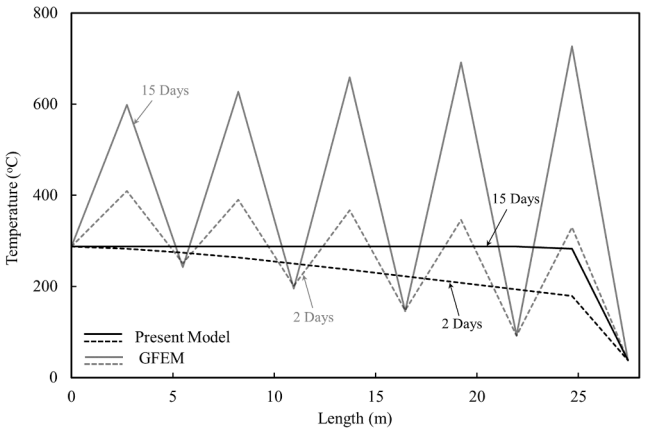

Fig. 8. Temperature profiles at different times at the center line of the reservoir for the case with $Pe = 160$ using the present model and GFEM.

(11) into the results, one obtains:

$$dn_w = \frac{dn_w}{dp_c}dp_c + \frac{dn_w}{dT}dT = n_w^{'}(dp_n - dp_w) + n_{wT}^{'}dT \tag{18}$$

$$dn_n = dn - dn_w = -(1-n)\boldsymbol{m}^T d\boldsymbol{\varepsilon} - n_w^{'}(dp_n - dp_w) - \left[(1-n)\beta_s + n_{wT}^{'}\right]dT \tag{19}$$

where $n_w^{'} = \frac{\partial n_w}{\partial p_c}$ and $n_{wT}^{'} = \frac{\partial n_w}{\partial T}$.

Substituting Eqs. (4), (5), (13), (18) and (19) into (12), the final form of the mass balance equations are obtained:

$$\left[n_w\frac{\partial \rho_w}{\partial p_w} - \rho_w n_w^{'}\right]\frac{D^s p_w}{Dt} + \rho_w n_w^{'}\frac{D^s p_n}{Dt} + \left[n_w\frac{\partial \rho_w}{\partial T} + \rho_w n_{wT}^{'}\right]\frac{D^s T}{Dt}$$
$$+\nabla^T\left\{\rho_w\frac{k_{rw}\boldsymbol{K}}{\mu_w}[\rho_w\boldsymbol{g} - \nabla p_w]\right\} + \rho_w n_w \boldsymbol{m}^T\mathcal{L}\frac{D^s\boldsymbol{u}}{Dt} - \dot{M}_w = 0 \tag{20}$$

$$\left[n_n\frac{\partial \rho_n}{\partial p_n} - \rho_n n_w^{'}\right]\frac{D^s p_n}{Dt} + \rho_n n_w^{'}\frac{D^s p_w}{Dt} + \left[n_n\frac{\partial \rho_n}{\partial T} - (1-n)\beta_s\rho_n - \rho_n n_{wT}^{'}\right]\frac{D^s T}{Dt}$$
$$+\nabla^T\left\{\rho_n\frac{k_m\boldsymbol{K}}{\mu_n}[\rho_n\boldsymbol{g} - \nabla p_n]\right\} + \rho_n(1-n+n_n)\boldsymbol{m}^T\mathcal{L}\frac{D^s\boldsymbol{u}}{Dt} - \dot{M}_n = 0 \tag{21}$$

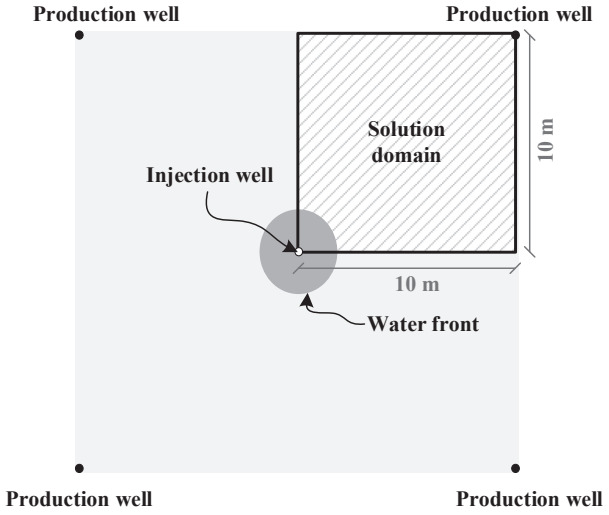

Fig. 9. The five-spot hot water flooding problem.

Table 4
Material properties for the five-spot problem.

Water density at reference condition, kg/m^3	$\rho_{w_{ref}} = 1000$
Oil density at reference condition, kg/m^3	$\rho_{o_{ref}} = 900$
Reference temperature, °C	$T_{ref} = 15.5$
Reference pressure, kPa	$p_{ref} = 101$
Rock porosity, %	$n = 37.5$
Water compressibility, vol/vol.kPa	$K_w = 21.37$
Oil compressibility, vol/vol.kPa	$K_o = 34.47$
Absolute permeability, m^2	$K = 1.3 \times 10^{-10}$
Specific heat capacity of water, J/kg.K	$C_w = 4184$
Specific heat capacity of oil, J/kg.K	$C_o = 2092$
Heat capacity of rock, kJ/ m^3.K	$\rho_s C_s = 2413$
Thermal conductivity of the mixture, W/m.K	$\chi = 0.1661$

2.2. Linear momentum balance equations

For any representative elementary volume (REV) of the mixture, the linear momentum balance equation for a quasi-static process can be written as:

$$\mathcal{L}^T\boldsymbol{\sigma} - \rho\boldsymbol{g} = 0 \tag{22}$$

where $\boldsymbol{\sigma}$ and ρ are the total stress and total density of the mixture, respectively:

$$\boldsymbol{\sigma} = \boldsymbol{\sigma}^{'} + \frac{1}{n}\boldsymbol{m}(n_w p_w + n_n p_n) \tag{23}$$

$$\rho = (1-n)\rho_s + \sum_{\alpha\neq s} n_\alpha\rho_\alpha \tag{24}$$

where $\boldsymbol{\sigma}^{'}$ is the effective stress which can be linked to the deformation of the skeleton through a general thermo-mechanical constitutive relation:

$$d\boldsymbol{\sigma}^{'} = \boldsymbol{D}^e\left(d\boldsymbol{\varepsilon} - d\boldsymbol{\varepsilon}_m^p - d\boldsymbol{\varepsilon}_T^e - d\boldsymbol{\varepsilon}_T^p\right) \tag{25}$$

where $\boldsymbol{D}^e$ is the elastic stiffness matrix, and $\boldsymbol{\varepsilon}_m^p$, $\boldsymbol{\varepsilon}_T^e$ and $\boldsymbol{\varepsilon}_T^p$ stand for the mechanical plastic strain, thermal elastic strain and thermal plastic strain of the skeleton, respectively. According to the observations of Campanella and Mitchell (1968), the thermal elastic strain of the soil skeleton can be assumed equal to that of the soil particles. Thus:

$$d\boldsymbol{\varepsilon}_T^e = -\frac{\boldsymbol{m}}{3}\beta_s dT \tag{26}$$

where β_s is defined in Eq. (10). The thermal and mechanical plastic strains ($\boldsymbol{\varepsilon}_m^p$ and $\boldsymbol{\varepsilon}_T^p$) can be calculated through an appropriate thermo-elastic-plastic constitutive model. Although such a model is not implemented in the present study, the formulation is developed in a way that makes it straight forward for future development.

Substituting Eq. (23) into (22), the final form of the linear momentum balance equation is obtained:

$$\mathcal{L}^T\boldsymbol{\sigma}^{'} + \mathcal{L}^T\boldsymbol{m}\frac{n_w}{n}p_w + \mathcal{L}^T\boldsymbol{m}\frac{n_n}{n}p_n - \rho\boldsymbol{g} = 0 \tag{27}$$

2.3. Energy balance equation

By enforcing the local thermal equilibrium assumption, a single energy balance equation is adequate to describe the heat transfer process in the multiphase mixture. This assumption implies that all the phases at each spatial point reaches thermal equilibrium instantaneously together.

Neglecting kinetic energy as well as viscous and intrinsic dissipations, the energy balance equation for any REV of the mixture can be written as:

Table 5
Water saturation and relative permeability for the five-spot problem.

s_w	k_{rw}	k_{ro}	p_c(kPa)
0.1	0.0	1.0	28.32
0.2	0.0016	0.875	0.65
0.3	0.0081	0.735	0.50
0.4	0.0259	0.59	0.42
0.5	0.0672	0.42	0.35
0.6	0.1000	0.21	0.28
0.7	0.1400	0.07	0.21
0.8	0.2000	0.016	0.14
0.86	0.2500	0.0	0.08

Table 6
Viscosity of the fluids for the five-spot problem.

T, ^{0}C	μ_w, cP	μ_o, cP
20	1.14	1200
40	0.63	250
60	0.45	155
80	0.35	70
100	0.29	38
120	0.25	23
140	0.22	15
160	0.19	10
180	0.18	7.5

$$\rho C\frac{D^s T}{Dt}+\bar{\boldsymbol{v}}^{*T}\nabla T-\nabla^T(\boldsymbol{\chi}\nabla T)-\rho h=0 \tag{28}$$

where:

$$\rho C=(1-n)\rho_s C_s+n_w\rho_w C_w+n_n\rho_n C_n \tag{29}$$

$$\rho h=(1-n)\rho_s h_s+n_w\rho_w h_w+n_n\rho_n h_n \tag{30}$$

$$\boldsymbol{\chi}=(1-n)\boldsymbol{\chi}_s+n_w\boldsymbol{\chi}_w+n_n\boldsymbol{\chi}_n \tag{31}$$

$$\bar{\boldsymbol{v}}^*=n_w\rho_w C_w\bar{\boldsymbol{v}}_w+n_n\rho_n C_n\bar{\boldsymbol{v}}_n \tag{32}$$

h_α, $C_\alpha$and $\boldsymbol{\chi}_\alpha$ are the external heat source/sink term, specific heat capacity and thermal conductivity tensor of phase α, respectively.

2.4. Initial and boundary conditions

Eqs. (20), (21), (27) and (28) represent a set of partial differential equations (on a domain Ω bounded by Γ), which are highly nonlinear and strongly coupled. The fluids pressure, p_w and p_n, skeleton deformation, $\boldsymbol{u}$, and temperature, T, are selected as the primary unknown variables. In order to reach a closed-form system of equations, the initial and boundary conditions associated with the primary variables are needed to be defined. The initial condition should specify the variables at time $t=0$:

$$\begin{cases} p_\alpha=p_\alpha^0,\ \alpha\neq s \\ \boldsymbol{u}=\boldsymbol{u}^0 \\ T=T^0 \end{cases} \quad \text{at } t=0,\ \text{on } \Omega \text{ and } \Gamma \tag{33}$$

Dirichlet boundary conditions are imposed as prescribed values of the primary variables:

$$\begin{cases} p_\alpha=\bar{p}_\alpha,\ \alpha\neq s & \text{on } \Gamma_{p_\alpha} \\ \boldsymbol{u}=\bar{\boldsymbol{u}} & \text{on } \Gamma_u \\ T=\bar{T} & \text{on } \Gamma_T \end{cases} \tag{34}$$

and Neumann boundary conditions are imposed as prescribed fluxes and tractions:

$$\begin{cases} \bar{q}_\alpha=\left\{\rho_\alpha\dfrac{k_{r\alpha}\boldsymbol{K}}{\mu_\alpha}[\rho_\alpha\boldsymbol{g}-\nabla p_\alpha]\right\}^T.\boldsymbol{n},\ \alpha\neq s & \text{on } \Gamma_{q_\alpha} \\ \bar{\boldsymbol{t}}=\boldsymbol{l}^T\boldsymbol{\sigma} & \text{on } \Gamma_t \\ \bar{q}=\{-\boldsymbol{\chi}\nabla T\}^T.\boldsymbol{n} & \text{on } \Gamma_q \end{cases} \tag{35}$$

where $\bar{q}_\alpha$ is the imposed mass flux of phase α, $\bar{\boldsymbol{t}}$ is the imposed traction, $\bar{q}$ is the imposed heat flux, $\boldsymbol{n}$ denotes the unit outward normal vector to the boundary:

$$\boldsymbol{n}=\{\,n_x\quad n_y\quad n_z\,\}^T \tag{36}$$

and the matrix $\boldsymbol{l}$ is defined as:

$$\boldsymbol{l}=\begin{bmatrix} n_x & 0 & 0 & n_y & 0 & n_z \\ 0 & n_y & 0 & n_x & n_z & 0 \\ 0 & 0 & n_z & 0 & n_y & n_x \end{bmatrix}^T \tag{37}$$

The conditions $\Gamma_{p_w}\cup\Gamma_{q_w}=\Gamma$, $\Gamma_{p_n}\cup\Gamma_{q_n}=\Gamma$, $\Gamma_u\cup\Gamma_t=\Gamma$ and $\Gamma_T\cup\Gamma_q=\Gamma$ should hold on the complementary parts of the boundary.

3. Numerical solution

Hexahedral elements are employed in this work to discretize the physical domain. The field variables $(p_w,p_n,\boldsymbol{u},T)$ are interpolated in terms of their corresponding nodal values $(\boldsymbol{p_w},\boldsymbol{p_n},\boldsymbol{U},\boldsymbol{T})$:

$$p_w=\boldsymbol{N}\boldsymbol{p_w},\ p_n=\boldsymbol{N}\boldsymbol{p_n},\ \boldsymbol{u}=\overline{\boldsymbol{N}}\boldsymbol{U},\ T=\boldsymbol{N}\boldsymbol{T} \tag{38}$$

where $\boldsymbol{N}$is the finite element shape functions for interpolating the pressure and temperature fields, and $\overline{\boldsymbol{N}}$ for the displacement field.

In Eq. (38) different shape functions have been used for the displacement field. This is a requirement when approaching the undrained limit state, where the permeability and compressibility matrixes are approaching to zero. In such a limiting case, the Babuska-Brezzi convergence conditions (Babuška, 1971, 1973; Brezzi, 1974) put some restrictions on the interpolating functions for pressure ($\boldsymbol{N}$) and displacement ($\overline{\boldsymbol{N}}$). The possible choices of elements to satisfy the necessary convergence and consistency criteria of the undrained limit are discussed by Zienkiewicz (1984). However, if the undrained limit state is never imposed, equal-order interpolations can be used without any problem (Lewis and Schrefler, 1998).

3.1. Mass balance equations – CVFEM

In order to derive the CVFE formulation of the mass balance equations (20) and (21) through a procedure similar to the FEM, the following weighting functions, $\boldsymbol{W}$, are considered:

$$W_i=H(\xi.\xi_i).H(\eta.\eta_i).H(\zeta.\zeta_i) \tag{39}$$

where ξ,η,ζ are the standard natural (local) coordination system of the element, the subscript i denotes the element nodes, and H is the Heaviside function:

$$H(x)=\begin{cases} 1 & x\geqslant 0 \\ 0 & x<0 \end{cases} \tag{40}$$

This weighting function implicitly divides the element into subdomains belonging to each node. This is known as the *subdomain collection technique*. Fig. 1-a shows the subdomain associated with node *i*. As shown in the figure, there are internal surfaces (abcd, abef, bcfg), namely internal boundaries (Γ_{int}), that separate this subdomain from the rest of the element.

The fundamental properties of the Heaviside function include (Stewart and Devenport, 2017):

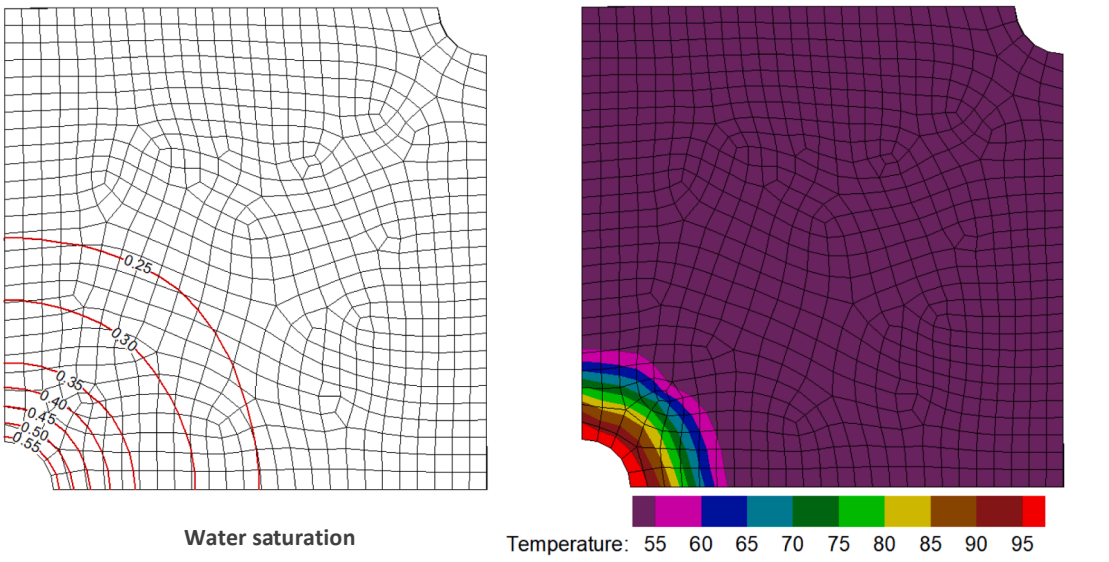

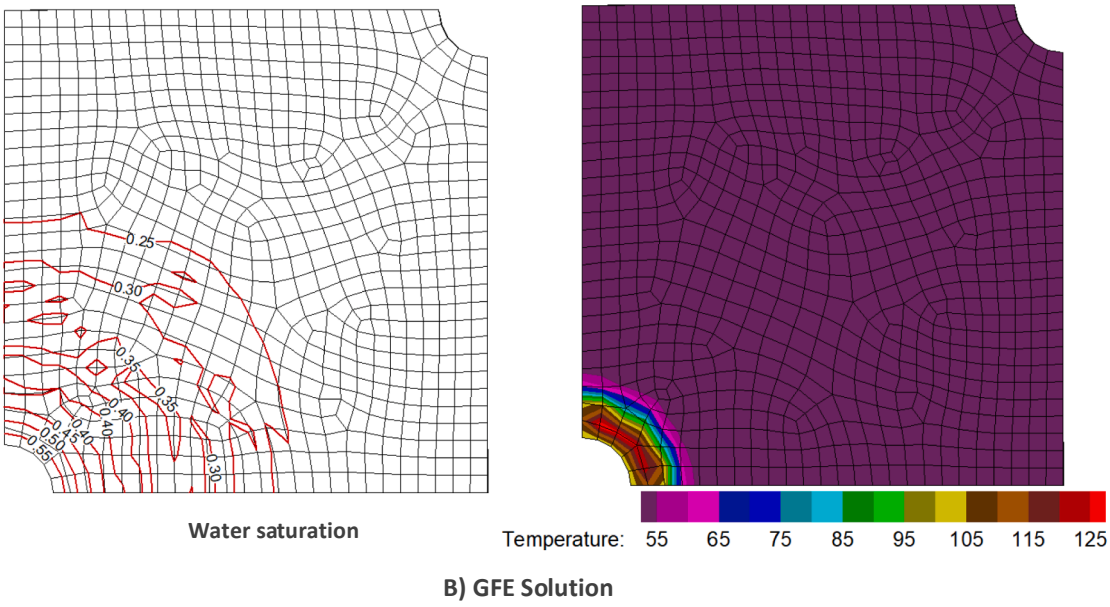

Fig. 10. Water saturation and temperature contours after 52 h of hot water injection; A) present model; and B) GFE solution.

$$\int_{\Omega_e} \boldsymbol{W}^T \nabla^T \boldsymbol{F} d\Omega = \int_{\Omega_s} [\boldsymbol{1}]^T \nabla^T \boldsymbol{F} d\Omega = \int_{\Gamma_s} [\boldsymbol{1}]^T \boldsymbol{F}^T . \boldsymbol{n} d\Gamma$$
$$= \int_{\Gamma_e} \boldsymbol{W}^T \boldsymbol{F}^T . \boldsymbol{n} d\Gamma + \int_{\Gamma_{int}} \boldsymbol{W}^T \boldsymbol{F}^T . \boldsymbol{n} d\Gamma \quad (41)$$

$$\int_{\Omega_e} (\nabla \boldsymbol{W})^T \boldsymbol{F} d\Omega = \int_{\Omega_e} \left[\nabla^T (\boldsymbol{F}\boldsymbol{W})\right]^T d\Omega - \int_{\Omega_e} \boldsymbol{W}^T \nabla^T \boldsymbol{F} d\Omega$$
$$= \int_{\Gamma_e} \boldsymbol{W}^T \boldsymbol{F}^T . \boldsymbol{n} d\Gamma - \int_{\Gamma_e} \boldsymbol{W}^T \boldsymbol{F}^T . \boldsymbol{n} d\Gamma - \int_{\Gamma_{int}} \boldsymbol{W}^T \boldsymbol{F}^T . \boldsymbol{n} d\Gamma = -\int_{\Gamma_{int}} \boldsymbol{W}^T \boldsymbol{F}^T . \boldsymbol{n} d\Gamma \quad (42)$$

where Ω_e and Ω_s are the domain of the element and the subdomain, respectively, that are bounded by Γ_e and Γ_s, while in this case $\boldsymbol{F}$ denotes a smooth vector field.

Considering Eq. (41), the weighted residual formulation of Eqs. (20) and (21) over Ω_e and Eq. (35) over Γ_e, can be written as:

$$\int_{\Omega_e} \boldsymbol{W}^T \left[n_w \frac{\partial \rho_w}{\partial p_w} - \rho_w n_w^{'} \right] \frac{D^s p_w}{Dt} d\Omega + \int_{\Omega_e} \boldsymbol{W}^T \rho_w n_w^{'} \frac{D^s p_n}{Dt} d\Omega + \int_{\Omega_e} \boldsymbol{W}^T \left[n_w \frac{\partial \rho_w}{\partial T} + \rho_w n_{wT}^{'} \right] \frac{D^s T}{Dt} d\Omega$$
$$+ \int_{\Gamma_e} \boldsymbol{W}^T \left\{ \rho_w \frac{k_{rw}\boldsymbol{K}}{\mu_w} [\rho_w \boldsymbol{g} - \nabla p_w] \right\}^T . \boldsymbol{n} d\Gamma + \int_{\Gamma_{\text{int}}} \boldsymbol{W}^T \left\{ \rho_w \frac{k_{rw}\boldsymbol{K}}{\mu_w} [\rho_w \boldsymbol{g} - \nabla p_w] \right\}^T . \boldsymbol{n} d\Gamma \quad (43)$$
$$+ \int_{\Omega_e} \boldsymbol{W}^T \rho_w n_w \boldsymbol{m}^T \mathcal{L} \frac{D^s \boldsymbol{u}}{Dt} d\Omega - \int_{\Omega_e} \boldsymbol{W}^T \dot{M}_w d\Omega + \int_{\Gamma_e} \boldsymbol{W}^T \left[\overline{q}_w - \left\{ \rho_w \frac{k_{rw}\boldsymbol{K}}{\mu_w} [\rho_w \boldsymbol{g} - \nabla p_w] \right\}^T . \boldsymbol{n} \right] d\Gamma = 0$$

$$\int_{\Omega_e} \boldsymbol{W}^T \left[n_n \frac{\partial \rho_n}{\partial p_n} - \rho_n n_w^{'} \right] \frac{D^s p_n}{Dt} d\Omega + \int_{\Omega_e} \boldsymbol{W}^T \rho_n n_w^{'} \frac{D^s p_w}{Dt} d\Omega$$
$$+ \int_{\Omega_e} \boldsymbol{W}^T \left[n_n \frac{\partial \rho_n}{\partial T} - (1-n)\beta_s \rho_n - \rho_n n_{wT}^{'} \right] \frac{D^s T}{Dt} d\Omega + \int_{\Gamma_e} \boldsymbol{W}^T \left\{ \rho_n \frac{k_{rn}\boldsymbol{K}}{\mu_n} [\rho_n \boldsymbol{g} - \nabla p_n] \right\}^T . \boldsymbol{n} d\Gamma$$
$$+ \int_{\Gamma_{\text{int}}} \boldsymbol{W}^T \left\{ \rho_n \frac{k_{rn}\boldsymbol{K}}{\mu_n} [\rho_n \boldsymbol{g} - \nabla p_n] \right\}^T . \boldsymbol{n} d\Gamma + \int_{\Omega_e} \boldsymbol{W}^T \rho_n (1 - n + n_n) \boldsymbol{m}^T \mathcal{L} \frac{D^s \boldsymbol{u}}{Dt} d\Omega \quad (44)$$
$$- \int_{\Omega_e} \boldsymbol{W}^T \dot{M}_n d\Omega + \int_{\Gamma_e} \boldsymbol{W}^T \left[\overline{q}_n - \left\{ \rho_n \frac{k_{rn}\boldsymbol{K}}{\mu_n} [\rho_n \boldsymbol{g} - \nabla p_n] \right\}^T . \boldsymbol{n} \right] d\Gamma = 0$$

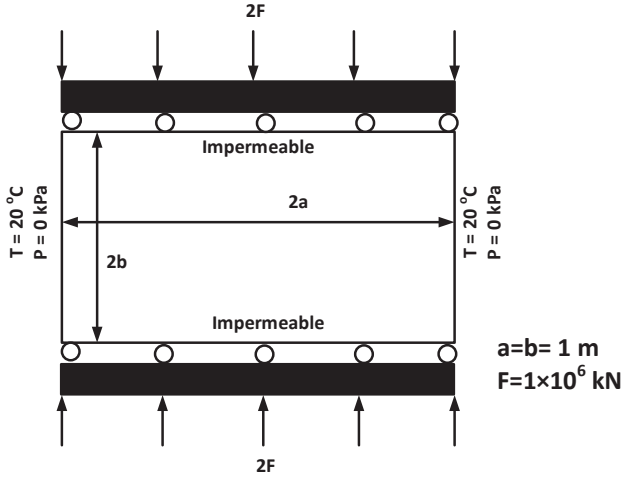

Fig. 11. The non-isothermal Mandel's problem: domain and boundary conditions.

As it can be seen, the internal boundaries appeared in the integral form of the partial differential equations. This is the main difference of the CVFE formulation comparing with the FEM.

Using the interpolatory representation of the field variables (Eq. (38)), the discretized form of the mass balance equations can be written as:

$$\overline{\boldsymbol{P}}_{ww} \boldsymbol{p}_w + \boldsymbol{P}_{ww} \frac{D^s \boldsymbol{p}_w}{Dt} + \boldsymbol{C}_{wn} \frac{D^s \boldsymbol{p}_n}{Dt} + \boldsymbol{C}_{wu} \frac{D^s \boldsymbol{U}}{Dt} + \boldsymbol{C}_{wT} \frac{D^s \boldsymbol{T}}{Dt} - \boldsymbol{f}_w = 0 \quad (45)$$

$$\overline{\boldsymbol{P}}_{nn} \boldsymbol{p}_n + \boldsymbol{C}_{nw} \frac{D^s \boldsymbol{p}_w}{Dt} + \boldsymbol{P}_{nn} \frac{D^s \boldsymbol{p}_n}{Dt} + \boldsymbol{C}_{nu} \frac{D^s \boldsymbol{U}}{Dt} + \boldsymbol{C}_{nT} \frac{D^s \boldsymbol{T}}{Dt} - \boldsymbol{f}_n = 0 \quad (46)$$

where the coefficients are listed below:

$$\overline{\boldsymbol{P}}_{ww} = -\int_{\Gamma_{\text{int}}} \boldsymbol{W}^T \left\{ \left(\rho_w \frac{k_{rw}\boldsymbol{K}}{\mu_w} \nabla \boldsymbol{N} \right)^T . \boldsymbol{n} \right\}^T d\Gamma \quad (47)$$

Table 7
Material properties for the non-isothermal Mandel's problem.

Shear modulus of the mixture, kPa	$G = 1 \times 10^6$
Poison ratio	$\nu = 0.2$
Absolute permeability, m^2	$K = 1 \times 10^{-9}$
Water viscosity, kPa.s	$\mu_w = 1 \times 10^{-6}$
Soil porosity, %	$n = 20$
Thermal conductivity of the mixture, W/m.K	$\chi = 5$
Thermal expansion of water, vol/vol.K	$\beta_w = 0.3 \times 10^{-6}$
Thermal expansion of soil, vol/vol.K	$\beta_s = 0.9 \times 10^{-6}$
Heat capacity of water, MJ/m^3.K	$\rho_w C_w = 4$
Heat capacity of soil, MJ/ m^3.K	$\rho_s C_s = 3$

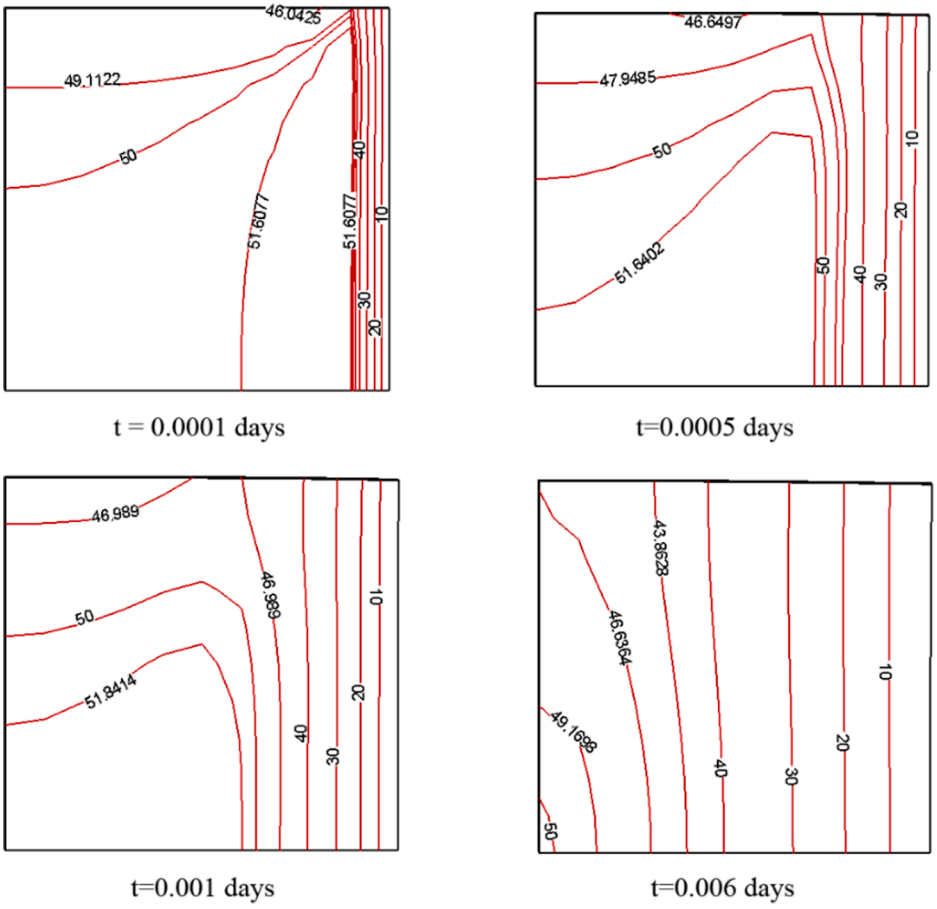

Fig. 12. Excess pore pressure at different time for the non-isothermal Mandel's problem.

$$\overline{\boldsymbol{P}}_{nn} = -\int_{\Gamma_{\text{int}}} \boldsymbol{W}^T \left\{ \left(\rho_n \frac{k_{rn}\boldsymbol{K}}{\mu_n} \nabla \boldsymbol{N} \right)^T .\boldsymbol{n} \right\}^T d\Gamma \tag{48}$$

$$\boldsymbol{P}_{ww} = \int_{\Omega_e} \boldsymbol{W}^T \left(n_w \frac{\partial \rho_w}{\partial p_w} - \rho_w n_w' \right) \boldsymbol{N} d\Omega \tag{49}$$

$$\boldsymbol{P}_{nn} = \int_{\Omega_e} \boldsymbol{W}^T \left(n_n \frac{d\rho_n}{dp_n} - \rho_n n_w' \right) \boldsymbol{N} d\Omega \tag{50}$$

$$\boldsymbol{C}_{wn} = \int_{\Omega_e} \boldsymbol{W}^T (\rho_w n_w') \boldsymbol{N} d\Omega \tag{51}$$

$$\boldsymbol{C}_{nw} = \int_{\Omega_e} \boldsymbol{W}^T (\rho_n n_w') \boldsymbol{N} d\Omega \tag{52}$$

$$\boldsymbol{C}_{wu} = \int_{\Omega_e} \boldsymbol{W}^T (\rho_w n_w) \boldsymbol{m}^T \boldsymbol{B} d\Omega \tag{53}$$

$$\boldsymbol{C}_{nu} = \int_{\Omega_e} \boldsymbol{W}^T (\rho_n (1-n) + \rho_n n_n) \boldsymbol{m}^T \boldsymbol{B} d\Omega \tag{54}$$

$$\boldsymbol{C}_{wT} = \int_{\Omega_e} \boldsymbol{W}^T \left(n_w \frac{\partial \rho_w}{\partial T} + \rho_w n_{wT}' \right) \boldsymbol{N} d\Omega \tag{55}$$

$$\boldsymbol{C}_{nT} = \int_{\Omega_e} \boldsymbol{W}^T \left(n_n \frac{\partial \rho_n}{\partial T} - (1-n)\beta_s \rho_n - \rho_n n_{wT}' \right) \boldsymbol{N} d\Omega \tag{56}$$

$$\boldsymbol{f}_w = \int_{\Omega_e} \boldsymbol{W}^T \dot{M}_w d\Omega - \int_{\Gamma_{q_w}} \boldsymbol{W}^T \overline{q}_w d\Gamma - \int_{\Gamma_{int}} \boldsymbol{W}^T \left[\rho_w^2 \left(\frac{k_{rw}\boldsymbol{K}}{\mu_w} \boldsymbol{g} \right)^T .\boldsymbol{n} \right] d\Gamma \tag{57}$$

$$\boldsymbol{f}_n = \int_{\Omega_e} \boldsymbol{W}^T \dot{M}_n d\Omega - \int_{\Gamma_{q_n}} \boldsymbol{W}^T \overline{q}_n d\Gamma - \int_{\Gamma_{int}} \boldsymbol{W}^T \left[\rho_n^2 \left(\frac{k_{rn}\boldsymbol{K}}{\mu_n} \boldsymbol{g} \right)^T .\boldsymbol{n} \right] d\Gamma \tag{58}$$

where $\boldsymbol{B}(= \mathcal{L}\overline{\boldsymbol{N}})$ is the strain-displacement matrix. Note that calculation of the volume and surface integrals follows the standard FEM practice.

The final set of the nodal mass balance equations can now be constructed using the standard assembling algorithm of the FEM. This will join the subdomains from all adjacent elements and form a bigger subdomain, namely control volume, around each node (Fig. 1-b). Considering the choice of the weighting functions in Eq. (39), all the integrals in Eqs. (45) and (46) will be automatically zero outside of the corresponding control volumes. It means, the mass balance equations are in fact satisfied in the control volumes, although they are presented at element level. In addition, the flux terms that are discontinues between the adjacent elements, are only appeared in surface integral terms on the internal boundaries (as shown in Eqs. (47) and (48)). Consequently, discontinuity of the velocity field between adjacent elements does not affect the local conservative characteristic of the calculations over the control volumes (Fig. 2). Indeed, construction of the control volumes is embedded in the formulation, thus there is no need to construct a dual mesh system. The discrete approximations follow the standard FE practice; the FEM data structure is retained, and the discrete equations are processed in elements loop.

3.2. Linear momentum balance equations – FEM

Applying the GFE discretization technique to Eq. (27) along with the boundary condition (Eq. (35)), the discretized form of the linear momentum balance equation can be derived:

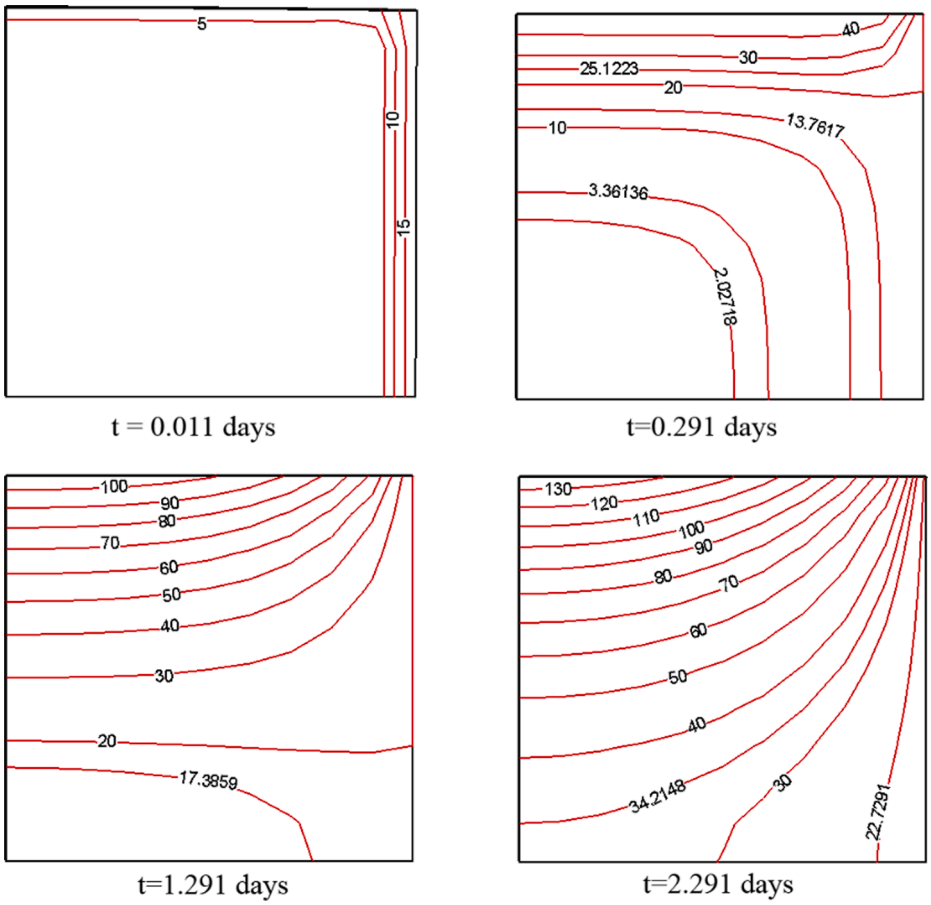

Fig. 13. Temperature profile at different time for the non-isothermal Mandel's problems.

$$\overline{\boldsymbol{C}}_{uw}\boldsymbol{p}_w + \overline{\boldsymbol{C}}_{un}\boldsymbol{p}_n + \boldsymbol{F}_{u-int} - \boldsymbol{f}_u = 0 \tag{59}$$

where the coefficients are listed below:

$$\overline{\boldsymbol{C}}_{uw} = \int_{\Omega_e} \frac{n_w}{n}\boldsymbol{B}^T\boldsymbol{m}\boldsymbol{N}d\Omega \tag{60}$$

$$\overline{\boldsymbol{C}}_{un} = \int_{\Omega_e} \frac{n_n}{n}\boldsymbol{B}^T\boldsymbol{m}\boldsymbol{N}d\Omega \tag{61}$$

$$\boldsymbol{F}_{u-int} = \int_{\Omega_e} \boldsymbol{B}^T\boldsymbol{\sigma}' d\Omega \tag{62}$$

$$\boldsymbol{f}_u = -\int_{\Omega_e} \overline{\boldsymbol{N}}^T\rho\boldsymbol{g}d\Omega + \int_{\Gamma_t} \overline{\boldsymbol{N}}^T\bar{\boldsymbol{t}}d\Gamma \tag{63}$$

3.3. Energy balance equation - SUCVFEM

In order to avoid the spurious oscillation of the temperature field in a convection-dominated problem, the weighting function of the CVFEM is modified in a way similar to the Petrov-Galerkin technique (Zienkiewicz et al., 2005):

$$\overline{\boldsymbol{W}} = \boldsymbol{W} + \boldsymbol{W}^* = \boldsymbol{W} + \frac{\theta h_e}{\sqrt{15}\|\bar{\boldsymbol{v}}^*\|}\bar{\boldsymbol{v}}^{*T}(\nabla\boldsymbol{W}) \tag{64}$$

where $\overline{\boldsymbol{W}}$ is the weighting function for the energy balance equation, $\boldsymbol{W}$ is defined in Eq. (39), h_e is the element characteristic length in the direction of flow (see the Appendix), and θ is defined as:

$$\theta = coth Pe - \frac{1}{Pe} \tag{65}$$

where Pe is the element Peclet number, defined as:

$$Pe = \frac{\|\bar{\boldsymbol{v}}^*\|h_e}{2\chi} \tag{66}$$

Weighting function of this type has been tested on a range of convection-diffusion problems by Swaminathan and Voller (1992).

The weighted residual formulation of the energy balance Eq. (28) over Ω_e and Eq. (35) over Γ_e, can now be written with the help of Eqs. (41) and (42):

$$\begin{aligned}&\int_{\Omega_e}\boldsymbol{W}^T\rho C\frac{D^sT}{Dt}d\Omega + \int_{\Omega_e}\boldsymbol{W}^T\bar{\boldsymbol{v}}^{*T}\nabla T d\Omega - \int_{\Gamma_e}\boldsymbol{W}^T(\chi\nabla T)^T.\boldsymbol{n}d\Gamma\\ &-\int_{\Gamma_{int}}\boldsymbol{W}^T(\chi\nabla T)^T.\boldsymbol{n}d\Gamma - \int_{\Omega_e}\boldsymbol{W}^T\rho h d\Omega + \int_{\Gamma_e}\boldsymbol{W}^T\left(\bar{q} + (\chi\nabla T)^T.\boldsymbol{n}\right)d\Gamma\\ &-\int_{\Gamma_{int}}\tau\boldsymbol{W}^T\bar{\boldsymbol{v}}^{*T}\left[\rho C\frac{D^sT}{Dt} + \bar{\boldsymbol{v}}^{*T}\nabla T - \nabla^T(\chi\nabla T) - \rho h\right]\boldsymbol{n}d\Gamma = 0\end{aligned} \tag{67}$$

where $\tau = \frac{\theta h_e}{\sqrt{15}\|\bar{\boldsymbol{v}}^*\|}$.

According to the discussion provided by Brooks and Hughes (1982), the effect of the perturbation weighting ($\boldsymbol{W}^*$) on the diffusion term ($\nabla^T(\chi\nabla T)$) can be neglected for regular shaped elements with first order basis functions. Following their argument, the discretized form of the energy balance equations can be written as:

$$\overline{\boldsymbol{T}}_{TT}\boldsymbol{T} + \boldsymbol{T}_{TT}\frac{D^s\boldsymbol{T}}{Dt} - \boldsymbol{f}_T = 0 \tag{68}$$

$$\overline{\boldsymbol{T}}_{TT} = \int_{\Omega_e}\boldsymbol{W}^T\bar{\boldsymbol{v}}^{*T}\nabla\boldsymbol{N}d\Omega - \int_{\Gamma_{int}}\boldsymbol{W}^T\left\{\left[(\chi\nabla\boldsymbol{N})^T + \tau\left(\bar{\boldsymbol{v}}^*\bar{\boldsymbol{v}}^{*T}\nabla\boldsymbol{N}\right)^T\right]\boldsymbol{n}\right\}^T d\Gamma \tag{69}$$

$$\boldsymbol{T}_{TT} = \int_{\Omega_e} \boldsymbol{W}^T \rho C N d\Omega - \int_{\Gamma_{int}} \tau \boldsymbol{W}^T \rho C N \overline{\boldsymbol{v}}^{*T} . \boldsymbol{n} d\Gamma \tag{70}$$

$$\boldsymbol{f}_T = \int_{\Omega_e} \boldsymbol{W}^T \rho h d\Omega - \int_{\Gamma_q} \boldsymbol{W}^T \overline{q} d\Gamma + \int_{\Gamma_{int}} \boldsymbol{W}^T \tau \rho h \overline{\boldsymbol{v}}^{*T} . \boldsymbol{n} d\Gamma \tag{71}$$

3.4. Temporal discretization

Spatial discretization of the governing equations has been carried out in the previous sections. The resulted Eqs. (45), (46), (59) and (68) represent a system of ordinary differential equations in time:

$$\begin{bmatrix} \boldsymbol{R}_{p_w} \\ \boldsymbol{R}_{p_n} \\ \boldsymbol{R}_U \\ \boldsymbol{R}_T \end{bmatrix} = \begin{bmatrix} \overline{\boldsymbol{P}}_{ww} & 0 & 0 & 0 \\ 0 & \overline{\boldsymbol{P}}_{nn} & 0 & 0 \\ \overline{\boldsymbol{C}}_{uw} & \overline{\boldsymbol{C}}_{un} & 0 & 0 \\ 0 & 0 & 0 & \overline{\boldsymbol{T}}_{TT} \end{bmatrix} \begin{bmatrix} \boldsymbol{p}_w \\ \boldsymbol{p}_n \\ \boldsymbol{U} \\ \boldsymbol{T} \end{bmatrix} + \begin{bmatrix} \boldsymbol{P}_{ww} & \boldsymbol{C}_{wn} & \boldsymbol{C}_{wu} & \boldsymbol{C}_{wT} \\ \boldsymbol{C}_{nw} & \boldsymbol{P}_{nn} & \boldsymbol{C}_{nu} & \boldsymbol{C}_{nT} \\ 0 & 0 & 0 & 0 \\ 0 & 0 & 0 & \boldsymbol{T}_{TT} \end{bmatrix} \frac{D^s}{Dt} \begin{bmatrix} \boldsymbol{p}_w \\ \boldsymbol{p}_n \\ \boldsymbol{U} \\ \boldsymbol{T} \end{bmatrix} + \begin{bmatrix} 0 \\ 0 \\ \boldsymbol{F}_{u-int} \\ 0 \end{bmatrix} - \begin{bmatrix} \boldsymbol{f}_w \\ \boldsymbol{f}_n \\ \boldsymbol{f}_u \\ \boldsymbol{f}_T \end{bmatrix} = 0 \tag{72}$$

The temporal discretization of similar systems is extensively discussed by many authors e.g. (Lewis and Schrefler, 1998; Peaceman, 1977; Schrefler and Xiaoyong, 1993; Schrefler et al., 1995; Settari and Aziz, 1979; Sukirman and Lewis, 1993), showing that the stability of the solution is strongly influenced by the approximation of the nonlinear terms in (72). They all concur that a fully implicit formulation is unconditionally stable. Following this recommendation, a fully implicit first order accurate finite difference scheme is adopted here for the temporal discretization of (72). It results in the following nonlinear equation:

$$\begin{bmatrix} \boldsymbol{R}_{p_w} \\ \boldsymbol{R}_{p_n} \\ \boldsymbol{R}_U \\ \boldsymbol{R}_T \end{bmatrix}_{n+1} = \begin{bmatrix} \boldsymbol{P}_{ww} + \Delta t . \overline{\boldsymbol{P}}_{ww} & \boldsymbol{C}_{wn} & \boldsymbol{C}_{wu} & \boldsymbol{C}_{wT} \\ \boldsymbol{C}_{nw} & \boldsymbol{P}_{nn} + \Delta t . \overline{\boldsymbol{P}}_{nn} & \boldsymbol{C}_{nu} & \boldsymbol{C}_{nT} \\ \overline{\boldsymbol{C}}_{uw} & \overline{\boldsymbol{C}}_{un} & 0 & 0 \\ 0 & 0 & 0 & \boldsymbol{T}_{TT} + \Delta t . \overline{\boldsymbol{T}}_{TT} \end{bmatrix}_{n+1} \begin{bmatrix} \boldsymbol{p}_w \\ \boldsymbol{p}_n \\ \boldsymbol{U} \\ \boldsymbol{T} \end{bmatrix}_{n+1} + \begin{bmatrix} 0 \\ 0 \\ \boldsymbol{F}_{u-int} \\ 0 \end{bmatrix}_{n+1} - \begin{bmatrix} \Delta t . \boldsymbol{f}_w \\ \Delta t . \boldsymbol{f}_n \\ \boldsymbol{f}_u \\ \Delta t . \boldsymbol{f}_T \end{bmatrix}_{n+1} - \begin{bmatrix} \boldsymbol{P}_{ww} & \boldsymbol{C}_{wn} & \boldsymbol{C}_{wu} & \boldsymbol{C}_{wT} \\ \boldsymbol{C}_{nw} & \boldsymbol{P}_{nn} & \boldsymbol{C}_{nu} & \boldsymbol{C}_{nT} \\ 0 & 0 & 0 & 0 \\ 0 & 0 & 0 & \boldsymbol{T}_{TT} \end{bmatrix}_{n+1} \begin{bmatrix} \boldsymbol{p}_w \\ \boldsymbol{p}_n \\ \boldsymbol{U} \\ \boldsymbol{T} \end{bmatrix}_n = 0 \tag{73}$$

where $\Delta t = t_{n+1} - t_n$ is the time step increment, and the subscripts n and $n+1$ denote time steps.

3.5. Linearization and solution strategy

Linearization of the system is performed using the Newton-Raphson algorithm. By expanding Eq. (73) with the first-order truncated Taylor series, the following linear approximation can be obtained:

$$\boldsymbol{J}^i_{n+1} \begin{bmatrix} \Delta \boldsymbol{p}_w \\ \Delta \boldsymbol{p}_n \\ \Delta \boldsymbol{U} \\ \Delta \boldsymbol{T} \end{bmatrix}^{i+1}_{n+1} = - \begin{bmatrix} \boldsymbol{R}_{p_w} \\ \boldsymbol{R}_{p_n} \\ \boldsymbol{R}_U \\ \boldsymbol{R}_T \end{bmatrix}^{i}_{n+1} \tag{74}$$

where the superscripts denote iterations, and $\boldsymbol{J}$ is the well-known Jacobian matrix. By solving the linearized system in Eqs. (74) in each iteration, the increment of the nodal degrees of freedom will be obtained, and then the corresponding nodal value will be updated as:

$$\begin{bmatrix} \boldsymbol{p}_w \\ \boldsymbol{p}_n \\ \boldsymbol{U} \\ \boldsymbol{T} \end{bmatrix}^{i+1}_{n+1} = \begin{bmatrix} \boldsymbol{p}_w \\ \boldsymbol{p}_n \\ \boldsymbol{U} \\ \boldsymbol{T} \end{bmatrix}^{i}_{n+1} + \begin{bmatrix} \Delta \boldsymbol{p}_w \\ \Delta \boldsymbol{p}_n \\ \Delta \boldsymbol{U} \\ \Delta \boldsymbol{T} \end{bmatrix}^{i+1}_{n+1} \tag{75}$$

This iterative procedure continues until the residual vector, $\boldsymbol{R}$, vanishes within the given tolerance. The Jacobian matrix is defined as $\partial \boldsymbol{R}^i_{n+1} / \partial \boldsymbol{X}^i_{n+1}$, which in this work is approximated as follows:

$$\boldsymbol{J}^i_{n+1} \simeq \begin{bmatrix} \boldsymbol{P}_{ww} + \Delta t . \left(\overline{\boldsymbol{P}}_{ww} + \widetilde{\boldsymbol{P}}_{ww} \right) & \boldsymbol{C}_{wn} + \Delta t . \widetilde{\boldsymbol{C}}_{wn} & \boldsymbol{C}_{wu} & \boldsymbol{C}_{wT} + \Delta t . \widetilde{\boldsymbol{C}}_{wT} \\ \boldsymbol{C}_{nw} + \Delta t . \widetilde{\boldsymbol{C}}_{nw} & \boldsymbol{P}_{nn} + \Delta t . \left(\overline{\boldsymbol{P}}_{nn} + \widetilde{\boldsymbol{P}}_{nn} \right) & \boldsymbol{C}_{nu} & \boldsymbol{C}_{nT} + \Delta t . \widetilde{\boldsymbol{C}}_{nT} \\ \overline{\boldsymbol{C}}_{uw} + \widetilde{\boldsymbol{C}}_{uw} & \overline{\boldsymbol{C}}_{un} + \widetilde{\boldsymbol{C}}_{un} & \widetilde{\boldsymbol{K}}_{uu} & \widetilde{\boldsymbol{C}}_{uT} \\ 0 & 0 & 0 & \boldsymbol{T}_{TT} + \Delta t . \overline{\boldsymbol{T}}_{TT} \end{bmatrix}^{i}_{n+1} \tag{76}$$

in which the partial derivatives are approximated as:

$$\widetilde{\boldsymbol{P}}_{ww} = \frac{\partial \overline{\boldsymbol{P}}_{ww}}{\partial \boldsymbol{p}_w} \boldsymbol{p}_w \simeq \int_{\Gamma_{int}} \boldsymbol{W}^T \left\{ \left(\rho_w \frac{\boldsymbol{K}}{\mu_w} \frac{\partial k_{rw}}{\partial n_w}' n_w p_w \nabla \boldsymbol{N} \right)^T . \boldsymbol{n} \right\}^T d\Gamma \tag{77}$$

$$\widetilde{\boldsymbol{C}}_{wn} = \frac{\partial \overline{\boldsymbol{P}}_{ww}}{\partial \boldsymbol{p}_n} \boldsymbol{p}_w \simeq - \int_{\Gamma_{int}} \boldsymbol{W}^T \left\{ \left(\rho_w \frac{\boldsymbol{K}}{\mu_w} \frac{\partial k_{rw}}{\partial n_w}' n_w p_w \nabla \boldsymbol{N} \right)^T . \boldsymbol{n} \right\}^T d\Gamma \tag{78}$$

$$\widetilde{\boldsymbol{C}}_{wT} = \frac{\partial \overline{\boldsymbol{P}}_{ww}}{\partial \boldsymbol{T}} \boldsymbol{p}_w \simeq - \int_{\Gamma_{int}} \boldsymbol{W}^T \left\{ \left(\rho_w \frac{\boldsymbol{K}}{\mu_w} \frac{\partial k_{rw}}{\partial n_w}' n_{wT} p_w \nabla \boldsymbol{N} \right)^T . \boldsymbol{n} \right\}^T d\Gamma \tag{79}$$

$$\widetilde{\boldsymbol{C}}_{nw} = \frac{\partial \overline{\boldsymbol{P}}_{nn}}{\partial \boldsymbol{p}_w} \boldsymbol{p}_n \simeq \int_{\Gamma_{int}} \boldsymbol{W}^T \left\{ \left(\rho_n \frac{\boldsymbol{K}}{\mu_n} \frac{\partial k_{rn}}{\partial n_w}' n_w p_n \nabla \boldsymbol{N} \right)^T . \boldsymbol{n} \right\}^T d\Gamma \tag{80}$$

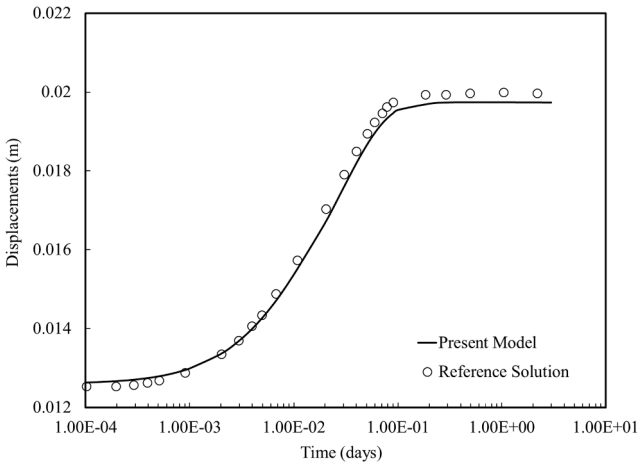

Fig. 14. Displacement, excess pore pressure and temperature evolutions at the center of the sample, compared to Pao et al. (2001).

$$\widetilde{\boldsymbol{P}}_{nn} = \frac{\partial \overline{\boldsymbol{P}}_{nn}}{\partial \boldsymbol{p}_n}\boldsymbol{p}_n \simeq -\int_{\Gamma_{\text{int}}} \boldsymbol{W}^T \left\{ \left(\rho_n \frac{\boldsymbol{K}}{\mu_n} \frac{\partial k_{rn}}{\partial n_w} n_w' p_n \nabla \boldsymbol{N} \right)^T . \boldsymbol{n} \right\}^T d\Gamma \tag{81}$$

$$\widetilde{\boldsymbol{C}}_{nT} = \frac{\partial \overline{\boldsymbol{P}}_{nn}}{\partial \boldsymbol{T}}\boldsymbol{p}_n \simeq -\int_{\Gamma_{\text{int}}} \boldsymbol{W}^T \left\{ \left(\rho_n \frac{\boldsymbol{K}}{\mu_w} \frac{\partial k_{rw}}{\partial n_w} n_{wT}' p_n \nabla \boldsymbol{N} \right)^T . \boldsymbol{n} \right\}^T d\Gamma \tag{82}$$

$$\widetilde{\boldsymbol{C}}_{uw} = \frac{\partial \overline{\boldsymbol{C}}_{uw}}{\partial \boldsymbol{p}_w}\boldsymbol{p}_w + \frac{\partial \overline{\boldsymbol{C}}_{un}}{\partial \boldsymbol{p}_w}\boldsymbol{p}_n = \int_{\Omega_e} \boldsymbol{B}^T \frac{n_w'}{n} \boldsymbol{m} p_c \boldsymbol{N} d\Omega \tag{83}$$

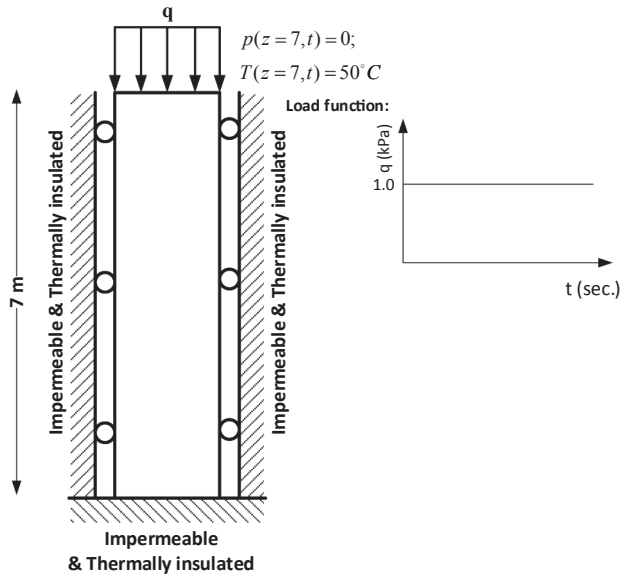

Fig. 15. The non-isothermal consolidation problem: domain and boundary conditions.

$$\widetilde{\boldsymbol{C}}_{un} = \frac{\partial \overline{\boldsymbol{C}}_{uw}}{\partial \boldsymbol{p}_n}\boldsymbol{p}_w + \frac{\partial \overline{\boldsymbol{C}}_{un}}{\partial \boldsymbol{p}_n}\boldsymbol{p}_n = -\int_{\Omega_e} \boldsymbol{B}^T \frac{n_w'}{n} \boldsymbol{m} p_c \boldsymbol{N} d\Omega \tag{84}$$

$$\begin{aligned} \widetilde{\boldsymbol{K}}_{uu} &= \frac{\partial \boldsymbol{F}_{u-int}}{\partial \boldsymbol{U}} + \frac{\partial \overline{\boldsymbol{C}}_{uw}}{\partial \boldsymbol{U}}\boldsymbol{p}_w + \frac{\partial \overline{\boldsymbol{C}}_{un}}{\partial \boldsymbol{U}}\boldsymbol{p}_n \\ &= \int_{\Omega_e} \boldsymbol{B}^T \left(-\boldsymbol{D}^e + \frac{n_w(1-n)}{n^2} \boldsymbol{m}.p_c \boldsymbol{m}^T \right) \boldsymbol{B} d\Omega \end{aligned} \tag{85}$$

$$\begin{aligned} \widetilde{\boldsymbol{C}}_{uT} &= \frac{\partial \boldsymbol{F}_{u-int}}{\partial \boldsymbol{T}} + \frac{\partial \overline{\boldsymbol{C}}_{uw}}{\partial \boldsymbol{T}}\boldsymbol{p}_w + \frac{\partial \overline{\boldsymbol{C}}_{un}}{\partial \boldsymbol{T}}\boldsymbol{p}_n \\ &\simeq \int_{\Omega_e} \boldsymbol{B}^T \left(\frac{\beta_s}{3} \boldsymbol{D}^e - \frac{n_{wT}'}{n} p_c - \frac{n_w}{n^2}(1-n)\beta_s p_c \right) \boldsymbol{m} \boldsymbol{N} d\Omega \end{aligned} \tag{86}$$

4. Numerical examples

The hydraulic part and the coupled hydro-mechanical part of the presented model have been previously published and extensively validated through several benchmark problems (Ghoreishian Amiri et al., 2017, 2013; Sadrnejad et al., 2012). Thus, in this work, the focus would be on the thermal coupling part to justify the performance of the presented THM formulation.

Table 8
Material properties for the non-isothermal consolidation problem.

Elastic modulus of the mixture, kPa	$E = 6 \times 10^3$
Poison ratio	$\nu = 0.4$
Water density, ton/m^3	$\rho_w = 1$
Soil density, ton/m^3	$\rho_s = 2$
Air density at initial condition, ton/m^3	$\rho_a = 1.22 \times 10^{-3}$
Bulk modulus of water, kPa	$K_w = 0.43 \times 10^{10}$
Absolute permeability, m^2	$K = 0.4 \times 10^{-12}$
Soil porosity, %	$n = 50$
Thermal conductivity of the mixture, kCal/m.K.s	$\chi = 0.2$
Thermal expansion of water, vol/vol.K	$\beta_w = 0.63 \times 10^{-5}$
Thermal expansion of soil, vol/vol.K	$\beta_s = 0.9 \times 10^{-6}$
Heat capacity of the mixture, kCal/ton.K	$C = 40 \times 10^3$
Viscosity of air, kPa.s	$\mu_a = 1 \times 10^{-9}$

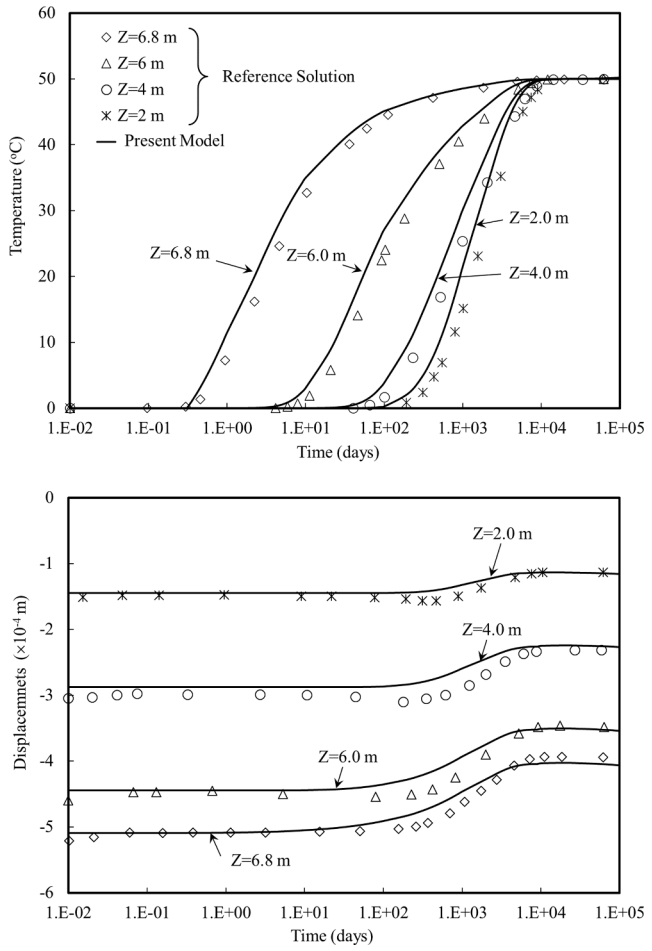

Fig. 16. Temperature and displacement evolutions at different depth, compared to Schrefler et al. (1995).

4.1. Natural convection

The buoyant flow in a differentially heated porous material has been considered in this example. The porous medium has been assumed to be non-deformable, and water saturated. This is a very well-known problem, where the fluid motion happens because of the temperature induced density variation. This problem has been extensively studied, and accurate solutions have been already presented (Oosthuizen, 2000).

The set-up of the problem is shown in Fig. 3, and the material properties are listed in Table 1. Water density varies with temperature according to the following relation:

$$\rho_w = \rho_{w_{\text{ref}}} + 2.57 \times 10^{-4}\left(T - T_{\text{ref}}\right) \tag{87}$$

where $\rho_{w_{\text{ref}}}$ denotes the density of water at a reference temperature, T_{ref}.

Numerical solutions in terms of streamlines and temperature isotherms are presented in Figs. 4 and 5, respectively. The qualitative comparison of the results obtained from the proposed model with those available in literature (Massarotti, 2001; Nithiarasu et al., 1997) shows a good agreement. The average Nusselt number,Nu_{avg}, along the hot wall has been used for quantitative comparison. The average Nusselt number represents the ratio between the total heat transfer to that in a pure conduction mode. In this case, it can be calculated as (Lewis et al., 2004):

$$\text{Nu}_{\text{avg}} = \frac{H}{L(T_h - T_c)} \int_0^L \frac{\partial T}{\partial x} dy \tag{88}$$

Table 2 provides the comparison of the predicted steady state average Nusselt number along the hot wall with those reported in literature.

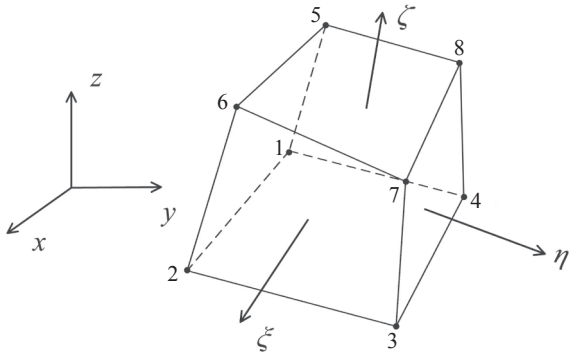

Fig. A1. General hexahedral element.

In order to show the efficiency of the solution in case of convection-dominated thermal flow, we have decreased the thermal conductivity of the system by a factor of 6, and re-analyzed the case. It results in an average Nusselt number of 2.357. The steady state results of this simulation are shown in Fig. 6.

4.2. Hot water injection

This example was first proposed by Aktan and Farouq-Ali (1978), and has been used by others (e.g. Pao et al. (2001)) for validation purposes. A Berea sandstone reservoir with a dimension of 9.15 m by 27.45 m (30 ft by 90 ft) and a thickness of 30.5 m (100 ft) has been considered. The reservoir was assumed to be fully saturated by water, with an initial pressure of 15170 kPa (2200 psia), and initial temperature of 37.8 °C (100 °F). The injection and production wells at the opposite ends of the reservoir operated under a constant pressure of 15,170 and 13790 kPa (2200 and 2000 psia), respectively. Injected water has a constant temperature of 287.8 °C (550 °F). Properties of rock and water for this problem are listed in Table 3. The following equations of state were used in the modelling:

$$\rho_w = \rho_{w_{\text{ref}}}\left[1 + K_w(p - p_{\text{ref}}) - \beta_w(T - T_{\text{ref}})\right] \tag{89}$$

$$\mu_w = 2.185/\left(0.000016701T^2 + 0.072809T + 0.289118\right) \tag{90}$$

where K_w and β_w denote the compressibility and thermal expansion of water, respectively. In Eq. (90), μ_w and T are given in cP and °C. The pressure and temperature profiles obtained from our simulation are compared, in Fig. 7, with those presented by Pao et al. (2001), and a remarkable agreement are observed.

In order to highlight the performance of the model in dealing with convection-dominated problems with high Peclet numbers, we have increased the absolute permeability of the medium by a factor of 20, and imposed a constant temperature of 37.8 °C at the production well. This results in a flow with a maximum Peclet number 160. The result from the present model is compared with GFEM in Fig. 8. As it is seen, the oscillatory results of the GFEM is eliminated in the present model by employing the SUCVFE scheme.

4.3. Five-spot hot water flooding

The problem analyzed in this section has been chosen from the literature of enhanced oil recovery. It is schematically depicted in Fig. 9. The physical domain is a homogenous porous material, initially saturated with 0.8 oil and 0.2 water. The initial temperature of the formation is 50 °C, while hot water at 100 °C is injected to the formation through the injection well at the constant pressure 1.79 MPa. A mixture of oil and water is recovered from the production wells at the constant pressure

1.31 MPa. The material properties for this problem are given in Tables 4–6. The problem was numerically solved by Sheorey and Muralidhar (2003). However, their saturation and temperature fields severely suffered from the so-called grid orientation effect (GOE) and spurious oscillation.

Fig. 10-A illustrates the results of the present model in terms of water saturation and temperature contours. As it is exhibited, the saturation isotherms are very smooth and not affected by orientation of the grids. The temperature isotherms are also smooth, but very slightly affected by the distorted elements. This small GOE appeared because of the upwind technique implemented in the solution of the energy balance equation. This is the price has been paid to get rid of the spurious oscillation of the temperature field without mesh updating.

In order to show the superiority of the proposed solution over the standard FEM, the problem has been also analyzed using the standard FEM. The results are shown in Fig. 10-B. As expected, serious oscillations are observed in both saturation and temperature fields. The former is the result of the non-conservative characteristic of the GFEM, which has been completely solved in our solution by adopting the CVFE technique. The latter is a well-known issue of the GFE formulation in convection-dominated transport problems, which has been reasonably solved in our solution using the SUCVFE technique.

4.4. The non-isothermal Mandel's problem

The Mandel's thermo-poro-elasticity problem was suggested by Pao et al. (2001) as a benchmark problem for coupled THM models. The set-up of the problem is shown in Fig. 11, and the material properties are listed in Table 7. The impermeable plates, shown in the figure, is connected to a heat source which supplies the heat at 1000 MJ/day. The initial temperature has been assumed to be 0 °C, and the temperature at the side boundaries have been assumed to increase to the constant room temperature of 20 °C on the onset of loading. Since the problem is symmetric, only one quarter of the domain was simulated.

Figs. 12 and 13 illustrate the excess pore pressure and temperature contours at different time steps. The time-history results, in terms of displacement, excess pore pressure and temperature, at the center of the sample, are illustrated in Fig. 14. The comparison of the results with those presented by Pao et al. (2001), in Fig. 14, reveals an excellent agreement.

4.5. Non-isothermal consolidation

In order to examine the coupled THM behavior of the model in the presence of two phase fluid flow, a thermo-poro-elastic soil column problem, presented by Schrefler et al. (1995), has been considered. Fig. 15 shows the geometry and boundary conditions of the problem. The sample is initially saturated with 92% water and 8% air. The initial stress, air pressure and temperature are assumed to be zero, 1 atm and 273.2 K, respectively. The capillary-water content relation has been considered as:

$$p_c = p_a - p_w = 1.68\left[\frac{n_w - 0.06}{0.4963 - 0.06}\right]^{-\frac{1}{3}} \tag{91}$$

Water viscosity varies with temperature according to the following relation:

$$\mu_w = 661.12(T - 229)^{-1.562} \tag{92}$$

where T is given in K and μ_w in cP. The air density follows the perfect gas law. Other relevant material properties are listed in Table 8.

Fig. 16 compares the solution obtained from the presented model with those by Schrefler et al. (1995), in terms of displacement and temperature profiles, and a reasonable agreement is observed.

5. Conclusions

In this paper, a fully coupled model for the simulation of complex behavior of two-phase fluid flow and heat transfer in deformable porous media has been presented. The conservation equations of mass, linear momentum and energy, together with the hydraulic, mechanical and thermal constitutive relations, provide the basis for the multiphysics formulation of a multiphase geological system. The system has been spatially discretized using a fully coupled hybrid numerical method by means of CVFEM for fluid flow, GFEM for deformation, and SUCVFEM for heat flow equations. The discrete approximations follow the standard FE practice, and the FEM data structure is retained. The proposed solution satisfies the local and global conservation of mass, which have been demonstrated to be crucial in problems with distinct saturation shock front. A fully implicit first order accurate finite difference scheme has been employed for temporal discretization of the equations. The efficiency of the streamline upwind scheme, which has been employed for the heat flow equation, has been illustrated in the numerical examples dealing with convection-dominated heat transport problems. However, very small grid orientation dependency has been observed, that is inherent in upwind techniques. The superiority of the proposed hybrid solution over the GFEM has been demonstrated through numerical examples. Five benchmark problems have been chosen to illustrate the accuracy and efficiency of the computational algorithm, and reasonable results have been achieved comparing to reference numerical and analytical solutions.

CRediT authorship contribution statement

S.A. Ghoreishian Amiri: Conceptualization, Methodology, Software, Validation, Writing - original draft. **E. Taheri:** Software, Validation, Writing - review & editing. **A.A. Lavasan:** Validation, Writing - review & editing.

Declaration of Competing Interest

The authors declare that they have no known competing financial interests or personal relationships that could have appeared to influence the work reported in this paper.

Acknowledgement

This work was supported by the Research Council of Norway through its Centers of Excellence funding scheme, project number 262644 Porelab, and the German Research Foundation (DFG) through the Collaborative Research Center (SFB 837) subproject A5.

Appendix A. The element characteristic length

A general hexahedral element is used here to define the element characteristic length (Fig. A1). First, the three vectors joining the midpoints of the opposing faces of the element are introduced as:

$$\boldsymbol{h}_{\xi} = \frac{1}{4}[(\boldsymbol{x}_2 + \boldsymbol{x}_3 + \boldsymbol{x}_6 + \boldsymbol{x}_7) - (\boldsymbol{x}_1 + \boldsymbol{x}_4 + \boldsymbol{x}_5 + \boldsymbol{x}_8)]$$
$$\boldsymbol{h}_{\eta} = \frac{1}{4}[(\boldsymbol{x}_3 + \boldsymbol{x}_4 + \boldsymbol{x}_7 + \boldsymbol{x}_8) - (\boldsymbol{x}_1 + \boldsymbol{x}_2 + \boldsymbol{x}_5 + \boldsymbol{x}_6)] \quad \text{(A1)}$$
$$\boldsymbol{h}_{\zeta} = \frac{1}{4}[(\boldsymbol{x}_5 + \boldsymbol{x}_6 + \boldsymbol{x}_7 + \boldsymbol{x}_8) - (\boldsymbol{x}_1 + \boldsymbol{x}_2 + \boldsymbol{x}_3 + \boldsymbol{x}_4)]$$

The projections of $\boldsymbol{h}_{\xi}$, $\boldsymbol{h}_{\eta}$, $\boldsymbol{h}_{\zeta}$ in the direction of the velocity vector $\overline{\boldsymbol{v}}^*$ are then calculated as:

$$h_1 = \frac{\overline{\boldsymbol{v}}^* . \boldsymbol{h}_{\xi}}{\|\overline{\boldsymbol{v}}^*\|} \;;\; h_2 = \frac{\overline{\boldsymbol{v}}^* . \boldsymbol{h}_{\eta}}{\|\overline{\boldsymbol{v}}^*\|} \;;\; h_3 = \frac{\overline{\boldsymbol{v}}^* . \boldsymbol{h}_{\zeta}}{\|\overline{\boldsymbol{v}}^*\|} \quad \text{(A2)}$$

Finally, the element characteristic length is defined as:

$$h_e = |h_1| + |h_2| + |h_3| \quad \text{(A3)}$$

References

Abed, A.A., Sołowski, W.T., 2017. A study on how to couple thermo-hydro-mechanical behaviour of unsaturated soils: Physical equations, numerical implementation and examples. Comput. Geotech. 92, 132–155.

Aktan, T., Farouq-Ali, S.M., 1978. Finite-Element Analysis of Temperature and Thermal Stresses Induced by Hot Water Injection. SPE-5765-PA 18, 457-469.

Asadi, R., Ataie-Ashtiani, B., 2021. Hybrid finite volume-finite element methods for hydro-mechanical analysis in highly heterogeneous porous media. Comput. Geotech. 132, 103996.

Babuška, I., 1971. Error-bounds for finite element method. Numer. Math. 16, 322–333.

Babuška, I., 1973. The finite element method with Lagrangian multipliers. Numer. Math. 20, 179–192.

Brezzi, F., 1974. On the existence, uniqueness and approximation of saddle-point problems arising from Lagrangian multipliers. RAIRO Anal. Numér. 8, 129–151.

Brooks, A.N., Hughes, T.J.R., 1982. Streamline upwind/Petrov-Galerkin formulations for convection dominated flows with particular emphasis on the incompressible Navier-Stokes equations. Comput. Methods Appl. Mech. Eng. 32, 199–259.

Campanella, R., Mitchell, J., 1968. Influence of temperature variations on soil behavior. ASCE J. Soil Mech. Found. Eng. Divis. 94, 709–734.

Chen, Z., Huan, G., Wang, H., 2005. Simulation of a compositional model for multiphase flow in porous media. Numer. Methods Partial Different. Eq. 21, 726–741.

Cui, W., Potts, D.M., Zdravković, L., Gawecka, K.A., Taborda, D.M.G., 2018. An alternative coupled thermo-hydro-mechanical finite element formulation for fully saturated soils. Comput. Geotech. 94, 22–30.

Forsyth, P.A., 1990. A Control-Volume, Finite-Element Method for Local Mesh Refinement in Thermal Reservoir Simulation. SPE Reservoir Eng. 5, 561–566.

Fung, L.S.K., Hiebert, A.D., Nghiem, L.X., 1992. Reservoir Simulation With a Control-Volume Finite-Element Method. SPE Reservoir Eng. 7, 349–357.

Ghoreishian Amiri, S.A., Sadrnejad, S.A., Ghasemzadeh, H., 2017. A hybrid numerical model for multiphase fluid flow in a deformable porous medium. Appl. Math. Model. 45, 881–899.

Ghoreishian Amiri, S.A., Sadrnejad, S.A., Ghasemzadeh, H., Montazeri, G.H., 2013. Application of control volume based finite element method for solving the black-oil fluid equations. Pet. Sci. 10, 361–372.

Gottardi, G., Dall'Olio, D., 1992. A control-volume finite-element model for simulating oil-water reservoirs. J. Petrol. Sci. Eng. 8, 29–41.

Hassanizadeh, M., Gray, W.G., 1979a. General conservation equations for multi-phase systems: 1. Averaging procedure. Adv. Water Resour. 2, 131–144.

Hassanizadeh, M., Gray, W.G., 1979b. General conservation equations for multi-phase systems: 2. Mass, momenta, energy, and entropy equations. Adv. Water Resour. 2, 191–203.

Hassanizadeh, S.M., Gray, W.G., 1993. Thermodynamic basis of capillary pressure in porous media. Water Resour. Res. 29, 3389–3405.

Hughes, T.J.R., Engel, G., Mazzei, L., Larson, M.G., 2000. The Continuous Galerkin Method Is Locally Conservative. J. Comput. Phys. 163, 467–488.

Kelkar, S., Lewis, K., Karra, S., Zyvoloski, G., Rapaka, S., Viswanathan, H., Mishra, P.K., Chu, S., Coblentz, D., Pawar, R., 2014. A simulator for modeling coupled thermo-hydro-mechanical processes in subsurface geological media. Int. J. Rock Mech. Min. Sci. 70, 569–580.

Kim, J., 2018. Unconditionally stable sequential schemes for all-way coupled thermoporomechanics: Undrained-adiabatic and extended fixed-stress splits. Comput. Methods Appl. Mech. Eng. 341, 93–112.

Lauriat, G., Prasad, V., 1989. Non-Darcian effects on natural convection in a vertical porous enclosure. Int. J. Heat Mass Transf. 32, 2135–2148.

Lee, J., Kim, K.-I., Min, K.-B., Rutqvist, J., 2019. TOUGH-UDEC: A simulator for coupled multiphase fluid flows, heat transfers and discontinuous deformations in fractured porous media. Comput. Geosci. 126, 120–130.

Lewis, R.W., Nithiarasu, P., Seetharamu, K.N., 2004. Fundamentals of the Finite Element Method for Heat and Fluid Flow. John Wiley & Sons, Sussex, England.

Lewis, R.W., Schrefler, B.A., 1998. The finite element method in the static and dynamic deformation and consolidation of porous media. John Wiley.

Massarotti, N., 2001. Heat and mass transfer in a porous medium. Ph.D Dissertation. University of Wales, Swansea.

McTigue, D.F., 1986. Thermoelastic response of fluid-saturated porous rock. J. Geophys. Res. Solid Earth 91, 9533–9542.

Mello, U.T., Rodrigues, J.R.P., Rossa, A.L., 2009. A control-volume finite-element method for three-dimensional multiphase basin modeling. Mar. Pet. Geol. 26, 504–518.

Nishimura, S., Gens, A., Jardine, R.J., Olivella, S., 2009. THM-coupled finite element analysis of frozen soil: formulation and application. Géotechnique 59, 159–171.

Nithiarasu, P., Seetharamu, K.N., Sundararajan, T., 1997. Natural convective heat transfer in a fluid saturated variable porosity medium. Int. J. Heat Mass Transf. 40, 3955–3967.

Nunziato, J.W., Walsh, E.K., 1980. On ideal multiphase mixtures with chemical reactions and diffusion. Arch. Ration. Mech. Anal. 73, 285–311.

Oosthuizen, P.H., 2000. Natural convective heat transfer in porous-media-filled enclosures. In: Vafai, K. (Ed.), Handbook of Porous Media. Marcel Dekker, New York.

Pao, W.K.S., Lewis, R.W., Masters, I., 2001. A fully coupled hydro-thermo-poro-mechanical model for black oil reservoir simulation. Int. J. Numer. Anal. Meth. Geomech. 25, 1229–1256.

Passman, S.L., 1977. Mixtures of granular materials. Int. J. Eng. Sci. 15, 117–129.

Peaceman, D.W., 1977. A Nonlinear Stability Analysis for Difference Equations Using Semi-Implicit Mobility. SPE-5765-PA 17, 79-91.

Rutqvist, J., 2011. Status of the TOUGH-FLAC simulator and recent applications related to coupled fluid flow and crustal deformations. Comput. Geosci. 37, 739–750.

Rutqvist, J., Wu, Y.S., Tsang, C.F., Bodvarsson, G., 2002. A modeling approach for analysis of coupled multiphase fluid flow, heat transfer, and deformation in fractured porous rock. Int. J. Rock Mech. Min. Sci. 39, 429–442.

Sadrnejad, S.A., Ghasemzadeh, H., Ghoreishian Amiri, S.A., Montazeri, G.H., 2012. A control volume based finite element method for simulating incompressible two-phase flow in heterogeneous porous media and its application to reservoir engineering. Pet. Sci. 9, 485–497.

Schiffman, R.L., 1971. A thermoelastic theory of consolidation. In: Environmental and Geophysical Heat Transfer. American Society of Mechanical Engineers, pp. 78–84.

Schrefler, B.A., Xiaoyong, Z., 1993. A fully coupled model for water flow and airflow in deformable porous media. Water Resour. Res. 29, 155–167.

Schrefler, B.A., Zhan, X., Simoni, L., 1995. A coupled model for water flow, airflow and heat flow in deformable porous media. Int. J. Numer. Meth. Heat Fluid Flow 5, 531–547.

Settari, A., Aziz, K., 1979. Petroleum Reservoir Simulation.

Sheorey, T., Muralidhar, K., 2003. Isothermal and non-isothermal oil–water flow and viscous fingering in a porous medium. Int. J. Therm. Sci. 42, 665–676.

Stewart, G., Devenport, W., 2017. Aeroacoustics of Low Mach Number Flows: Fundamentals, Analysis and Measurement. Academic Press.

Sukirman, Y., Lewis, R.W., 1993. A finite element solution of a fully coupled implicit formulation for reservoir simulation. Int. J. Numer. Anal. Meth. Geomech. 17, 677–698.

Swaminathan, C.R., Voller, V.R., 1992. Streamline upwind scheme for control-volume finite elements, part II. Implementation and comparison with the SUPG finite-element scheme. Numer. Heat Transfer, Part B: Fundam. 22, 109–124.

Tong, F., Jing, L., Zimmerman, R.W., 2010. A fully coupled thermo-hydro-mechanical model for simulating multiphase flow, deformation and heat transfer in buffer material and rock masses. Int. J. Rock Mech. Min. Sci. 47, 205–217.

Verma, S., 1996. Flexible grids for reservoir simulation, Department of Petroleum Engineering. Ph.D Dissertation, University of Stanford.

Wan, J., 2002. Stabilized finite element methods for coupled geomechanics and multiphase flow. Ph.D Dissertation, Stanford University.

Wei, C., Muraleetharan, K.K., 2002. A continuum theory of porous media saturated by multiple immiscible fluids: I. Linear poroelasticity. Int. J. Eng. Sci. 40, 1807–1833.

Winterfeld, P.H., Wu, Y.-S., 2016. Simulation of Coupled Thermal/Hydrological/Mechanical Phenomena in Porous Media. SPE-173210-PA 21, 1041-1049.
Zhou, X., Ghassemi, A., 2009. Finite element analysis of coupled chemo-poro-thermo-mechanical effects around a wellbore in swelling shale. Int. J. Rock Mech. Min. Sci. 46, 769–778.
Zienkiewicz, O.C., 1984. In: Coupled Problems and their Numerical Solution, Numerical Methods in Coupled Systems. John Wiley and Sons Ltd, pp. 35–58.
Zienkiewicz, O.C., Taylor, R.L., Nithiarasu, P., 2005. The Finite Element Method for Fluid Dynamics, sixth ed. Elsevier Butterworth-Heinemann.